SAND2022-15828 R
LDRD PROJECT NUMBER: 226345
LDRD PROJECT TITLE: Narrow-linewidth laser cooling for rapid production of low-temperature atoms for high data-rate quantum sensing
PROJECT TEAM MEMBERS: Roger Ding, Adrian Orozco, Jongmin Lee, Neil Claussen

Sandia National Laboratories is a multimission laboratory managed and operated by National Technology and Engineering Solutions of Sandia, LLC, a wholly owned subsidiary of Honeywell International, Inc., for the U.S. Department of Energy's National Nuclear Security Administration under contract DE-NA-0003525.

LDRD LABORATORY DIRECTED RESEARCH & DEVELOPMENT
WHERE INNOVATION BEGINS

ABSTRACT:

We present a proof-of-concept demonstration of a narrow linewidth ^{87}Rb magneto-optical trap (MOT) operating on the narrow linewidth $5S_{1/2} \rightarrow 6P_{3/2}$ transition at 420 nm. We stabilized the absolute frequency of the 420 nm laser to an atomic transition in ^{87}Rb and demonstrate a MOT using 420 nm light driving the $5S_{1/2}, F = 2 \rightarrow 6P_{3/2}, F' = 3$ transition. We then use time-of-flight measurements to characterize the 420 nm MOT temperature, observing a minimum temperature of about $T_{horizontal}^{(420)} = 150$ μK and $T_{vertical}^{(420)} = 250$ μK before the opportunity to perform significant characterization and optimization. Although this temperature is significantly higher than the expected 420 nm Doppler cooling limit ($T_D^{(420)} \approx 34$ μK), these are already approaching the Doppler cooling limit of a standard 780 nm MOT ($T_D^{(780)} \approx 146$ μK). We believe that with further optimization the Doppler cooling limit of ≈ 34 μK can be achieved. This initial result answers our key research question and demonstrates the viability of applying narrow linewidth laser cooling as a robust technique for future fieldable quantum sensors.

INTRODUCTION AND EXECUTIVE SUMMARY OF RESULTS:

Introduction

The rapid and reliable generation of ultra-low-temperature atoms is critical for sophisticated next-generation quantum sensors including atom interferometer accelerometers/gyroscopes and gravimeters/gravity gradiometers [1-5], optical lattice clocks [6-9], and rapidly-developing neutral-atom quantum computing and simulation platforms [10-17]. As *the* tool for producing ultracold atoms, magneto-optical traps (MOTs) have proven to be robust with field demonstrations on terrestrial [18, 19], naval [20], airborne [21-24], and space [25, 26] platforms, but their ultimate achievable temperature is limited by the atomic linewidth (Γ) addressed by the cooling lasers, known as the Doppler cooling limit (T_D). These upcoming next-generation quantum sensors often require additional "sub-Doppler" cooling stages to reach sufficiently cold temperatures (e.g., polarization gradient cooling, Raman sideband cooling, or evaporative cooling) to mitigate effects of remaining atomic motion [27] and/or to reach quantum degeneracy. Although powerful, these sub-Doppler cooling techniques often require sophisticated equipment, exhibit high environmental sensitivity, and need additional time after the MOT, making them difficult to implement for real-world quantum sensing applications. In this report, our narrow linewidth MOT approach shows a potential path to improve the performance significantly without too much increase in complexity of the apparatus for deployable quantum sensors with ultracold atoms.

The Doppler cooling limit is given by $T_D = \hbar\Gamma/2k_B$ [28, 29] although reaching this limit in practice is typically difficult [30]. Focusing on rubidium (Rb), an important atom for quantum sensing efforts at Sandia and globally, the current state-of-the-art method is to use a 780 nm MOT with a linewidth of $\Gamma = 2\pi(6.06\text{ MHz})$ [31, 32], corresponding to $T_D \approx 146$ μK. Lower temperatures (approaching ~ 5 μK) are achievable with 780 nm sub-Doppler cooling techniques

[33-35], but these typically require extinction of the MOT quadrupole magnetic field, nulling of stray magnetic fields [36], and careful optimization of the intensity and detuning of the cooling beams. Absence of the MOT quadrupole magnetic field also means the atoms are no longer trapped during the sub-Doppler cooling time window. In addition, maintaining zero stray magnetic field requires heavy magnetic shielding and/or active cancellation, making the process challenging to implement outside the laboratory. Sub-Doppler cooling also adds a few-to-tens-of-milliseconds after the MOT stage; while this is relatively insignificant for ultracold and quantum degenerate gas experiments that operate with typical cycle times of about one second or more (e.g., [26, 37-39]) it becomes a significant limiting factor for high data rate operation when the cooling time restricts the achievable sensing duty cycle [40-42].

An alternative approach is to use a narrow linewidth transition to directly achieve lower sample temperatures since $T_D \propto \Gamma$. A significant advantage of a narrow linewidth MOT compared to sub-Doppler cooling is that the atoms remain trapped. Narrow linewidth laser cooling has been a crucial technique for producing ultracold gases of alkaline-earth-like elements (e.g., calcium [43, 44], strontium [45], ytterbium [46], cadmium [47]) and rare-earth elements (e.g., erbium [48], dysprosium [49], thulium [50]). For hydrogen-like alkali atoms, narrow linewidth cooling has been demonstrated using $nS_{1/2} \rightarrow (n+1)P_{3/2}$ transitions in lithium ($2S_{1/2} \rightarrow 3P_{3/2}$ at 323 nm [51-53]), potassium ($4S_{1/2} \rightarrow 5P_{3/2}$ at 405 nm [51, 54]), and rubidium ($5S_{1/2} \rightarrow 6P_{3/2}$ at 420 nm [55][1]).

Table 1. Comparison of expected ^{87}Rb Doppler cooling performance using the 780 nm $5S_{1/2} \rightarrow 5P_{3/2}$ transition vs. the 420 nm $5S_{1/2} \rightarrow 6P_{3/2}$ transition. Table follows the notation used in [56] where v (w) is the upper (lower) state.

v	w	λ [nm]	$\Gamma^{\mathrm{Expt}} = 1/\tau_v^{\mathrm{Expt}}$ [MHz]	T_D [μK]
$5P_{3/2}$	$5S_{1/2}$	780.241209686 [32]	6.06 [31]	146
$6P_{3/2}$	$5S_{1/2}$	420.298726885 [57]	1.42 [58]	34

Rubidium's $5S_{1/2} \rightarrow 6P_{3/2}$ transition at 420 nm has a linewidth of $\Gamma_{420\,\mathrm{nm}} \lesssim 2\pi(1.42\ \mathrm{MHz})$ [58, 59], meaning the Doppler cooling limit is expected to be about 34 μK, significantly lower than for the 780 nm transition (key values highlighted in Table 1). Although not as low as using 780 nm sub-Doppler cooling, the expected $T_{D,420\,\mathrm{nm}} \approx 34$ μK along with the lack of atom cloud expansion during sub-Doppler cooling will be highly beneficial for atom interferometry due to the greater initial cloud density and lower expansion rate at the outset of the atom interferometer Raman pulse sequence [41].

[1] The rubidium 420 nm MOT preprint [55] was submitted to arXiv during this LDRD.

LABORATORY DIRECTED RESEARCH & DEVELOPMENT
WHERE INNOVATION BEGINS

Executive Summary

We have demonstrated a narrow linewidth MOT driving the rubidium $5S_{1/2} \rightarrow 6P_{3/2}$ transition at 420 nm. This result is applicable towards advancing light-pulse atom interferometer (LPAI) technology to enable advanced positional awareness and GPS-denied navigation in DOE NNSA missions. Our study is aligned with "Position, Navigation, and Timing (PNT)" (gravity aided navigation and quantum inertial measurement units (IMUs)) and "Quantum Sensing (QS)" (gravimeters, accelerometers, gyroscopes, and gravity gradiometers). We showed the feasibility of the narrow linewidth MOT that can potentially eliminate the need for sub-Doppler cooling processes for LPAI-based quantum sensors.

In this LDRD, we have achieved our first key goal and made significant progress towards the second:

1. Demonstrate laser cooling and trapping of ^{87}Rb using the $5S_{1/2} \rightarrow 6P_{3/2}$ transition at 420 (i.e., a 420 nm MOT)
2. Show that the 420 nm MOT temperature is below the 780 nm Doppler cooling limit ($T_{D,780\text{ nm}} \approx 146$ μK)

Although we have not yet had the opportunity to improve the system and optimize the 420 nm MOT, these initial results showing $T_{420\text{ nm MOT}} \approx (150 - 250)$ μK are highly promising for future work towards achieving robust operation of a 420 nm MOT for fieldable quantum sensors.

DETAILED DESCRIPTION OF RESEARCH AND DEVELOPMENT AND METHODOLOGY:

Comparison of the 780 nm and 420 nm Cooling Transitions

In a standard ^{87}Rb MOT, a 780 nm cooling laser drives the $|5S_{1/2}, F = 2\rangle \rightarrow |5P_{3/2}, F' = 3\rangle$ cycling transition. Ideally, the $F = 2 \rightarrow F' = 3$ transition is closed but weak off-resonant scattering leads some atoms to decay into the lower $|5S_{1/2}, F = 1\rangle$ hyperfine level that is dark to the cooling light. A second 780 nm repump laser closes this leak and recycles atoms dark to the cooling laser by driving the $|5S_{1/2}, F = 1\rangle \rightarrow |5P_{3/2}, F' = 2\rangle$ from which they can then decay to the $|5S_{1/2}, F = 2\rangle$ and return to the cycling transition. Figure 1(a) provides a diagram of the relevant energy levels for a 780 nm MOT.

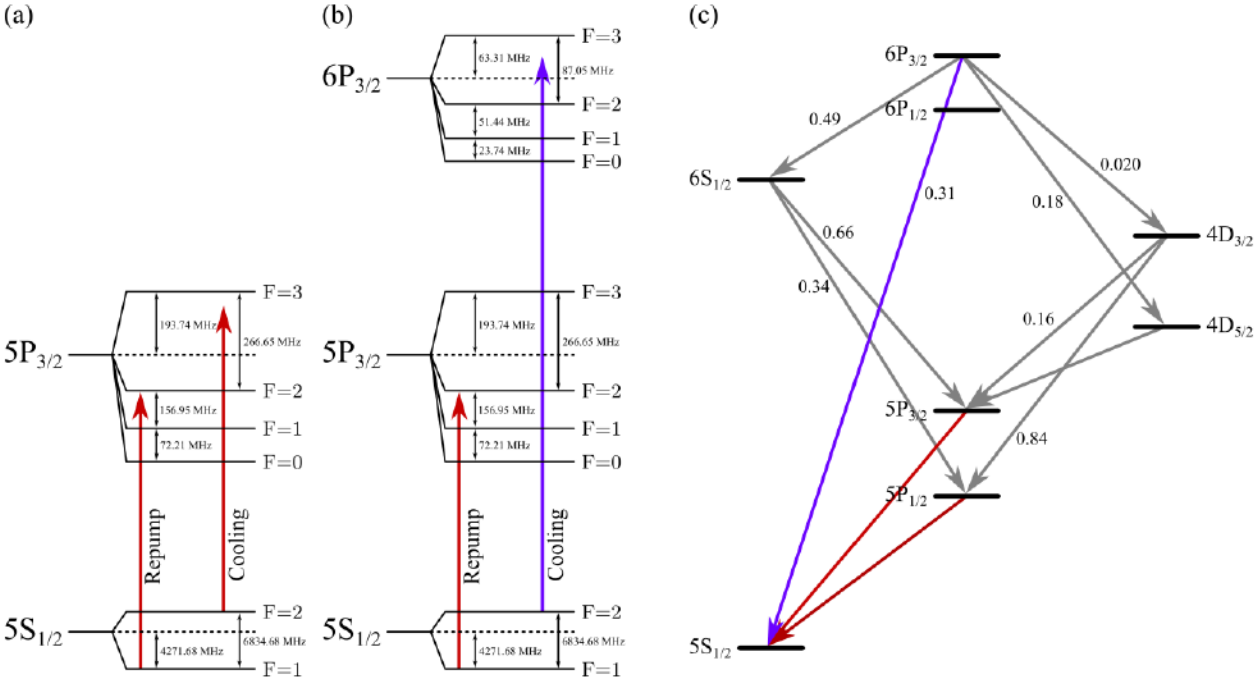

Figure 1. Partial energy level diagram of ^{87}Rb. Laser driven transitions for (a) the 780 nm MOT and (b) the 420 nm MOT (figure modified from [57] with energy splittings from [32, 57]). (c) Decay cascade from the $6P_{3/2}$ state with approximate branching ratios from [60].

Analogous to the 780 nm MOT, the 420 nm MOT replaces the 780 nm cooling laser with a 420 nm laser that drives the $|5S_{1/2}, F = 2\rangle \rightarrow |6P_{3/2}, F' = 3\rangle$ transition. In our setup, we did not have a modulator that could provide the ~ 6.568 GHz modulation so that a single 420 nm laser could also drive the $|5S_{1/2}, F = 1\rangle \rightarrow |6P_{3/2}, F' = 2\rangle$ transition to recycle atoms back to the upper $|5S_{1/2}, F = 2\rangle$ hyperfine state (i.e., a 420 nm repump laser). Instead, we rely on the 780 nm repump laser used for the 780 nm MOT similar to the schemes reported in [52, 54, 55]. Figure 1(b) shows our experimental laser scheme with a 420 nm cooling laser and a 780 nm repump. In principle, we should be able to make a MOT with an entirely 420 nm system (eliminating the 780 nm repump) as was demonstrated for Li [51-53].

Additional Details About the 420 nm Transition

From the reduced dipole matrix element $|\langle 5S_{1/2}\|D\|6P_{3/2}\rangle| = 0.541ea_0$ [56][2], the linewidth of the $5S_{1/2} \rightarrow 6P_{3/2}$ transition is expected to be $\Gamma \approx 2\pi(318\text{ kHz})$ corresponding to $T_D \approx 8\,\mu\text{K}$. But unlike the $5P_{3/2}$ which can only decay back to $5S_{1/2}$ by emission of a 780 nm photon, there are multiple possible decay paths from the $6P_{3/2}$ state (see Figure 1(c)). In particular, note that an excited atom follows the direct $6P_{3/2} \rightarrow 5S_{1/2}$ decay path via spontaneous emission of a 420

[2] Note that there is another common convention related by $\langle J\|D\|J'\rangle = \sqrt{2J+1}\langle J\|D\|J'\rangle$ [32].

nm photon only about 31% of the time [60]. An atom predominantly decays via multiphoton cascade through various intermediate states, reducing the lifetime of the $6P_{3/2}$ state to $\tau \approx$ 112 ns [56, 59] corresponding to a linewidth of $\Gamma \approx 2\pi(1.42\ \text{MHz})$ and resulting $T_D \approx 34\ \mu\text{K}$. Table 2 provides some values for comparison of the 780 nm and 420 nm transitions.

Table 2. Comparison of 780 nm and 420 nm transitions. Following from the notation used in [56] where v (w) is the upper (lower) state.

v	w	λ [nm]	$\lvert\langle v\rVert D\rVert w\rangle\rvert$ [ea_0]	τ_{vw} [ns]	$\frac{1}{2\pi\tau_{vw}}$ [MHz]	τ_v^{Expt} [ns]	$\frac{1}{2\pi\tau_v^{\text{Expt}}}$ [MHz]
$5P_{3/2}$	$5S_{1/2}$	780.241209686 [32]	5.956 [56]	26.434	6.021	26.25 [31]	6.063
$6P_{3/2}$	$5S_{1/2}$	420.298726885 [57]	0.541 [56]	500.809	0.318	112 [58]	1.421

Although the decay cascade effectively broadens the linewidth of 420 nm transition leading to a larger T_D, it could potentially enable higher density MOTs due to a reduction of antitrapping forces from atoms reradiating near-resonant cooling light as MOT density increases [61]. The multiple decay pathways could also lead to a lower Doppler cooling limit due to reduced momentum diffusion from emission of multiple long-wavelength photons instead of a single 420 nm photon [29].

Overview of 780 nm and 420 nm Magneto-Optical Traps (MOTs)

Laser cooling and trapping using magneto-optical traps (MOTs) have been extensively covered elsewhere (e.g., [29, 62, 63]) and we follow the same principles here for ^{87}Rb using the (standard) 780 nm and the (new) 420 nm transitions. Figure 2(a) shows the schematic of a 1D MOT driving a $J = 0 \rightarrow J' = 1$ transition in a two-level atom (a more complicated diagram for ^{87}Rb can be found in [64]). Figure 2(b) gives a qualitative picture of the 1D MOT forces driving the $|F = 2, m_F = +2\rangle \rightarrow |F' = 3, m_F' = +3\rangle$ transition at 780 nm and 420 nm.

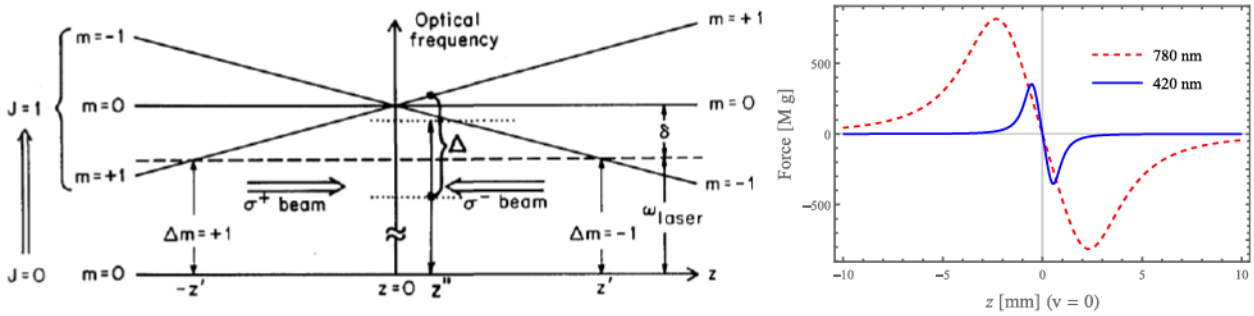

Figure 2. (a) Exemplary energy levels of a 1D MOT for a two-level atom driving $J = 0 \rightarrow J' = 1$ transition (figure from [65]). A quadrupole magnetic field shifts the $m = \pm 1$ states; σ^+ (σ^-) is a rightward (leftward) propagating circularly polarized laser; Δ is the laser detuning from zero-field resonance. (b) Simplified 1D MOT force calculation assuming a two-level atom driving the $|F = 2, m_F = +2\rangle \rightarrow |F' = 3, m_F' = +3\rangle$ transition for 780 nm

(red dashed line) and 420 nm (blue solid line) normalized by the gravitational force on a ^{87}Rb atom. Calculation parameters: $\Gamma_{780\,nm} = 2\pi(6\,MHz)$, $\Gamma_{420\,nm} = 2\pi(1.4\,MHz)$, $\Delta = -\Gamma/2$, $dB/dz = 10\,G/cm$, $s = 0.1$.

An approximate generalization for a 3D MOT can be achieved by treating it as three 1D MOTs along the orthogonal cartesian axes. A quantitative calculation of the forces in a 3D MOT is significantly more involved as one would need to project the laser polarizations on the local orientation of the quadrupole magnetic field although this could be accomplished using something like [66]. Figure 3(a) shows the setup for a 3D MOT using three-pairs of counterpropagating MOT beams to provide confinement and cooling in all spatial dimensions. Figure 3(b) depicts a two-color (dual-wavelength) MOT setup with both 780 nm and 420 nm MOT beams (MOT coils omitted). A quarter-waveplate (QWP) converts both 780 nm and 420 nm MOT beams to circularly polarized light with the same handedness.

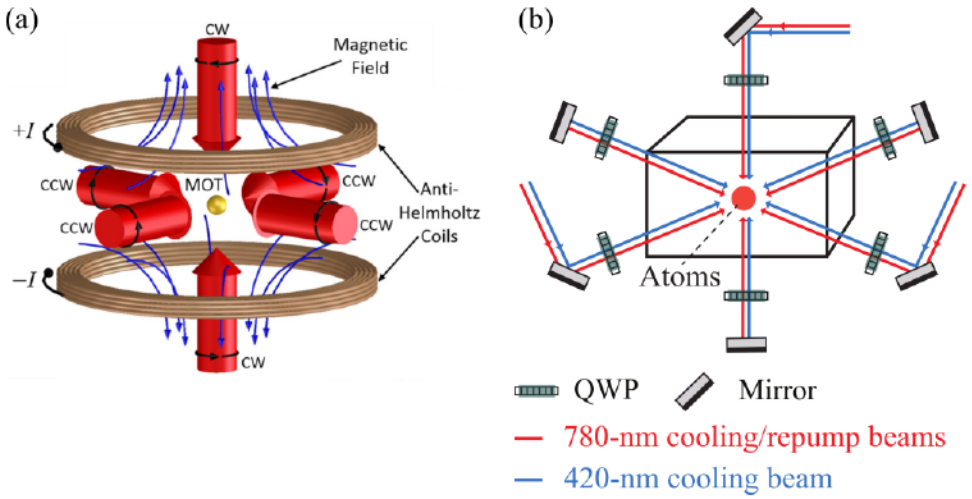

Figure 3. (a) Diagram of a single-wavelength 3D MOT (from [67]). (b) Two-color (dual-wavelength) 3D MOT with overlapping 780 nm and 420 nm MOT beams. MOT coils omitted for clarity. Custom quarter-waveplates (QWPs) convert both 780 nm and 420 nm beams to the same circular polarization. Drawn with some components from [68].

Experimental System

All the experiments occur inside the ultrahigh vacuum (UHV) system shown in Figure 4. The UHV system is based around an approximately $2 \times 1 \times 4$ inch^3 ($50.8 \times 25.4 \times 101.6$ mm^3) rectangular glass cell. Commercial-off-the-shelf Rb dispensers (SAES RB/NF/3.4/12FT10+10) were spot-welded to feedthroughs to produce the Rb vapor for laser cooling and trapping. An ion pump (5 L/s from HeatWave Labs) maintains the $\approx 3 \times 10^{-9}$ Torr vacuum with the Rb dispenser off.

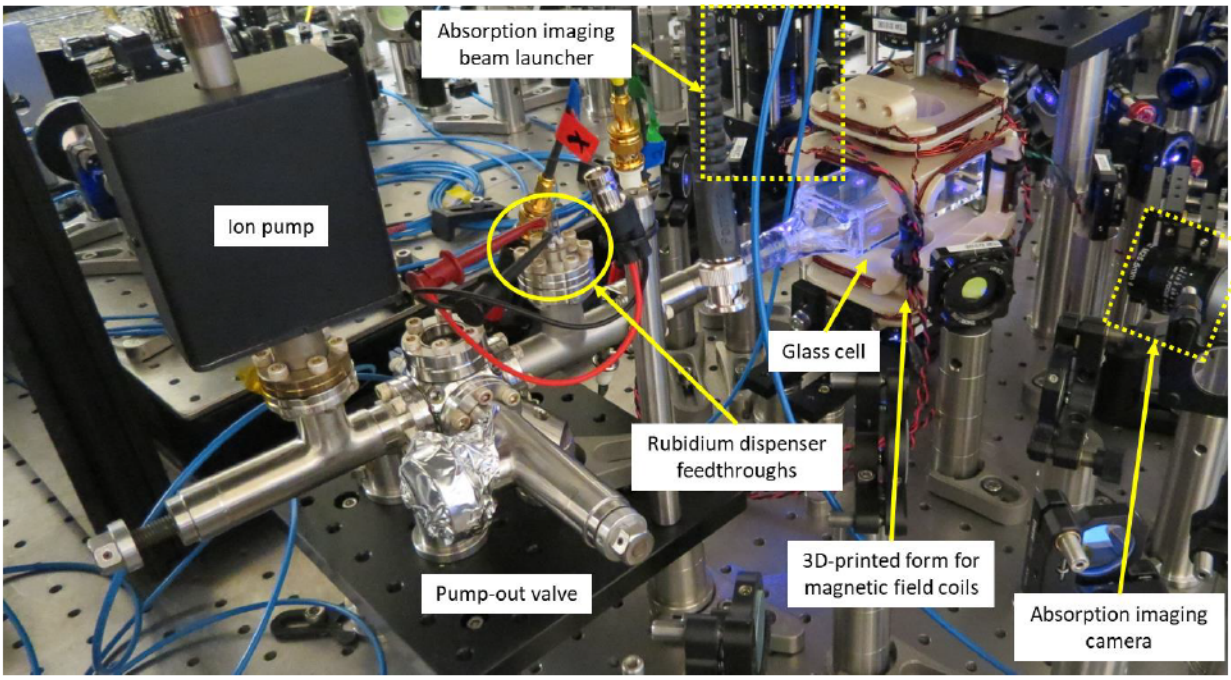

Figure 4. Picture of the vacuum system with the main components labeled.

Around the glass cell is a 3D-printed coil form that provides four (4) sets of magnetic field coils: a quadrupole anti-Helmholtz coil for MOT operation and three (3) sets of Helmholtz coils that provide some control of magnetic fields along three orthogonal axes.

Unexpected Challenge Due to the Glass Cell

While glass cells provide excellent optical access, the particular glass cell used for this work is antireflection (AR) coated for 780 nm but not for 420 nm. Table 3 shows the results of transmission measurements through the glass cell at 780 nm and 420 nm, indicating significant losses for the latter.

Table 3. Measurements of laser transmission through the glass cell. P_{In} is the power incident on the glass cell; P_{Out} is the power transmitted through the glass cell; T is the transmission coefficient per wall.

λ [nm]	P_{In} [mW]	P_{Out} [mW]	$T = \left(\frac{P_{\mathrm{Out}}}{P_{\mathrm{In}}}\right)^{\frac{1}{2}}$
780	4.07	3.7	0.953463
420	6.5	3.8	0.764601

For a laser transmitting through n walls, the transmission coefficient (T) per wall is

$$P_{\text{Out}} = T^n P_{\text{In}} \Rightarrow T = \left(\frac{P_{\text{Out}}}{P_{\text{In}}}\right)^{\frac{1}{n}}$$

where a "wall" is taken to be one exterior surface (air-to-glass interface) and one interior surface (glass-to-vacuum interface). In this situation, $n = 2$ since the lasers pass through one wall entering the vacuum chamber and another one exiting.

For 780 nm light, $T_{780\text{ nm}} \approx 95\%$ is consistent with one AR-coated surface (minimal transmission losses) and one non-AR-coated surface (typically expect about 5% loss). The AR-coated surface is very likely on the exterior of the glass cell. The $T_{780\text{ nm}}^2 \approx 91\%$ power imbalance is tolerable for the 780 nm MOT.

Due to a lack of knowledge of the coating specifications for the available glass cell at the outset of the project, the MOT design could not be validated until the 420 nm laser was delivered from the vendor in late May 2022. Once the laser was available, the glass cell's poor 420 nm transmission ($T_{420\text{ nm}} \approx 76\%$) was discovered, requiring us to significantly modify our MOT design. The initial plan was to use a simple three-beam retroreflected dual-color MOT configuration with both 780 nm and 420 nm copropagating (Figure 5(a)). Due to the low $T_{420\text{ nm}}$, the retroreflected 420 nm MOT beam would contain only about $T_{420\text{ nm}}^2 \approx 58\%$ of the first pass power, leading to a significant imbalance of the scattering forces. As a result, we had to redesign the 420 nm MOT optics to generate six independent MOT beams that were each individually overlapped with the retroreflecting 780 nm MOT beams (see Figure 5(b)).

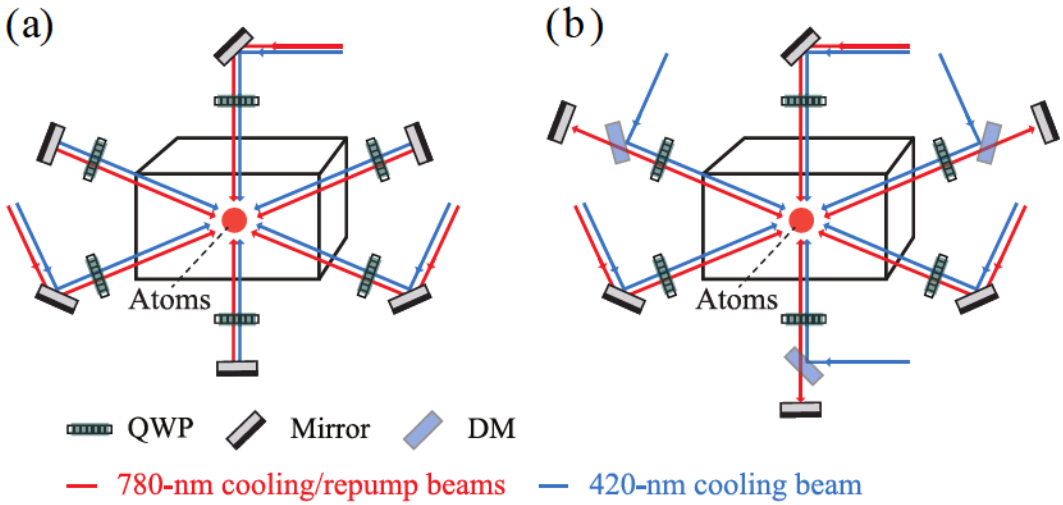

Figure 5. (a) Original design for a simple dual-wavelength (780 nm and 420 nm) three-beam retroreflected MOTs. (b) Modified setup using a three retroreflected 780 nm MOT beams and six independent 420 nm MOT beams. QWP: quarter-waveplate; DM: dichroic mirror transmitting 780 nm and reflecting 420 nm. Drawn with components from [68].

780 nm Laser System

The main 780 nm laser power comes from a revived laser system originally described in [69]. Starting from a 1560 nm narrow linewidth fiber seed laser (NP Photonics Rock RFLM-25-3-1560.49-1-S-V), the output is amplified to ~7 W by an erbium-doped fiber amplifier (EDFA, IPG EAR-10K-C-LP-SF). The EDFA output is delivered to the optical table where a periodically poled lithium niobate (PPLN) crystal produces 780 nm light via second harmonic generation (SHG) of 1560 nm light (see Figure 6(a)). This light is then split with about 25 mW directed to the Lock fiber input coupler for laser stabilization (Figure 6(b)) and the remaining light is delivered to the AOM Network fiber coupler for further modulation (see Figure 7).

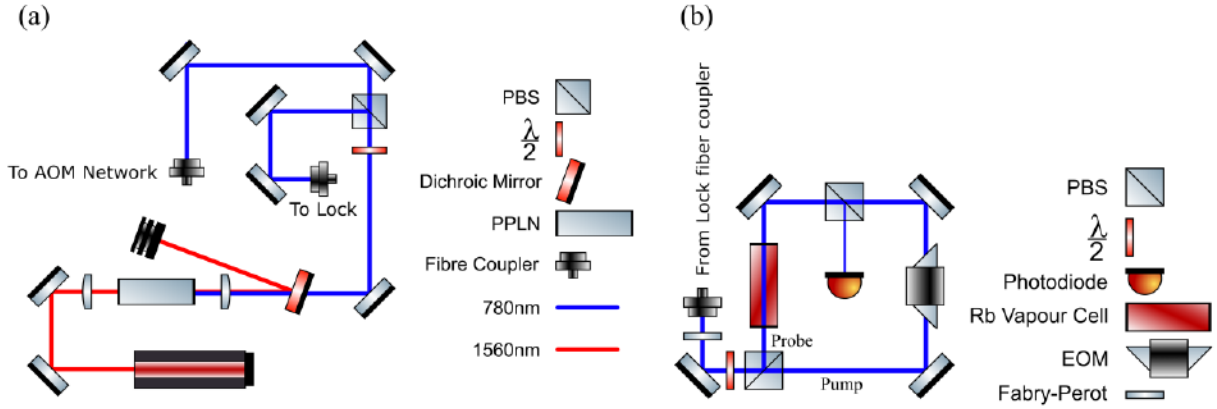

Figure 6. (a) Schematic of the main 1560 nm to 780 nm generation system. (b) Schematic of the modulation transfer spectroscopy (MTS) setup for stabilizing the 780 nm frequency. The fiber electro-optic modulator (fEOM) between the Lock input and output fiber couplers is omitted. Figures modified from [69] and drawn using components from [68].

Stabilization of the 780 nm laser system is achieved by using the modulation transfer spectroscopy (MTS) [70] setup shown in Figure 6(b). Not shown in Figure 6 is a fiber electro-optic modulator between the Lock input and output fiber couplers that enables a wide tuning range by locking to a radiofrequency (RF) tunable sideband instead of the carrier.

Most of the generated 780 nm light is fiber-coupled to an acousto-optic modulator (AOM) Network for frequency shifting and amplitude modulation (see Figure 7). The AOM Network features several double-pass AOMs that provides extended frequency-tuning ranges compared to single-pass setups [71]. In the current setup, only AOMs C1 and C2 are used. C1 provides an approximately $2 \times (-150.8\ \text{MHz})$ frequency shift for the MOT cooling light. C2 is operated at about $2 \times (-145\ \text{MHz})$ to provide resonant light for absorption imaging on the $|5S_{1/2}, F = 2\rangle \rightarrow |5P_{3/2}, F' = 3\rangle$ transition.

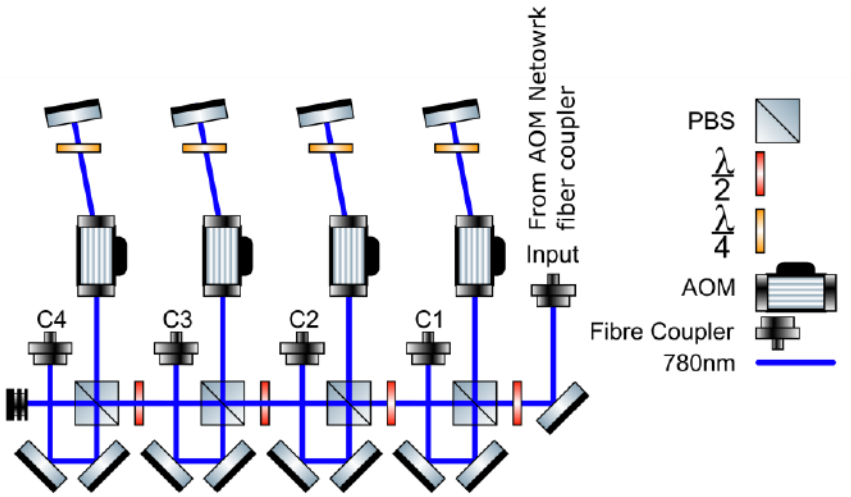

Figure 7. AOM Network for frequency shifting and amplitude modulation of 780 nm light. In the current setup, only C1 and C2 are used for MOT cooling and absorption imaging, respectively. Figure modified from [69] and drawn using components from [68].

A separate 780 nm distributed Bragg reflector (DBR) diode laser is independently locked to a rubidium saturated absorption cell to provide repump light. The laser current is modulated at about 4 MHz, resulting in a frequency modulated (FM) laser output. This is then used to perform FM spectroscopy on a rubidium vapor cell to obtain an error signal for locking to the $|5S_{1/2}, F = 1\rangle \rightarrow |5P_{3/2}, F' = 1{,}2\rangle$ crossover resonance. An AOM at about +78.5 MHz serves as an optical switch and provides the frequency shift to make the light delivered to the experiment resonant with $|5S_{1/2}, F = 1\rangle \rightarrow |5P_{3/2}, F' = 2\rangle$ transition for repumping.

The 780 nm cooling and repump light are coupled into polarization maintaining (PM) fibers for delivery to the experiment where they are launched with large-diameter fiber collimators (Thorlabs F810APC-780) that produce approximately 7.5 mm diameter beams, setting the size of the 780 nm MOT. The repump is aligned to copropagate with the cooling beam but with orthogonal polarization. The combined 780 nm cooling and repump light are then split into the three 780 nm MOT beams with a series of half-waveplates (HWPs) and PBSs (see Figure 8).

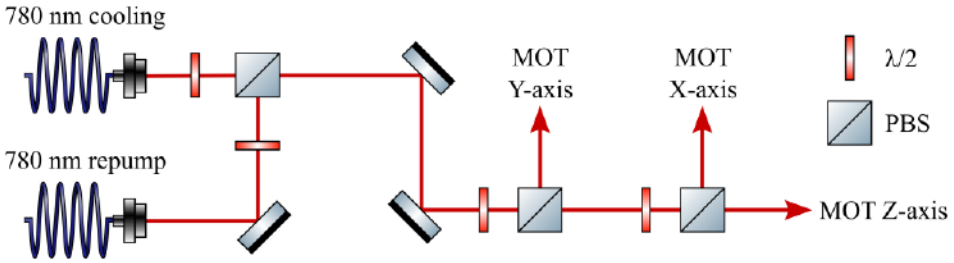

Figure 8. Schematic of the optics for combining the 780 nm cooling and repump MOT beams delivered via polarization maintaining (PM) fibers. The copropagating cooling and repump beams are split with a series of half-waveplates (HWPs) and polarizing beam splitters (PBSs) to generate the three 780 nm MOT beams. Drawn using [68].

420 nm Laser System

The 420 nm light comes from a commercial external cavity diode laser (ECDL, TOPTICA Photonics DL pro), providing about 55 mW of 420 nm light. As shown in Figure 9, the output beam quality of the 420 nm ECDL is quite poor. Mode cleaning by fiber coupling the 420 nm light was not pursued to maintain the maximum useable power. Figure 10 shows the schematic of the 420 nm laser system. Approximately 7 mW of light from the laser output is diverted for laser stabilization with the remaining light being used for the MOT.

Stabilizing the absolute frequency of the 420 nm ECDL begins by coupling a sample of the light into a single mode (SM) fiber connected to a wavemeter (Bristol 871A VIS) so that the correct lasing mode is selected. The rest of the beam is then expanded by about $2\times$ to increase the interaction volume of the spectroscopy beams with the rubidium atoms to obtain a larger signal. The light is then split by a polarizing beam splitter (PBS) with the transmitted light becoming the probe beam. The reflected light is directed towards a double-pass Lock AOM where the RF drive is modulated at about 100 kHz (lock-in amplifier reference signal) by jumping between -196 MHz and -204 MHz with an RF switch (Mini-Circuits ZASWA-2-50DR+). Due to the double-pass Lock AOM setup, the pump beam jumps between $2(-196\ \text{MHz}) = -392$ MHz and $2(-204\ \text{MHz}) = -408$ MHz. The probe and pump beams then counterpropagate through a rubidium vapor cell heated to about 65 C with orthogonal linear polarizations. The probe beam then passes through a 420 nm bandpass filter (Thorlabs FBH420-10) to reduce background light and is collected on a photodetector (Thorlabs PDA8A).

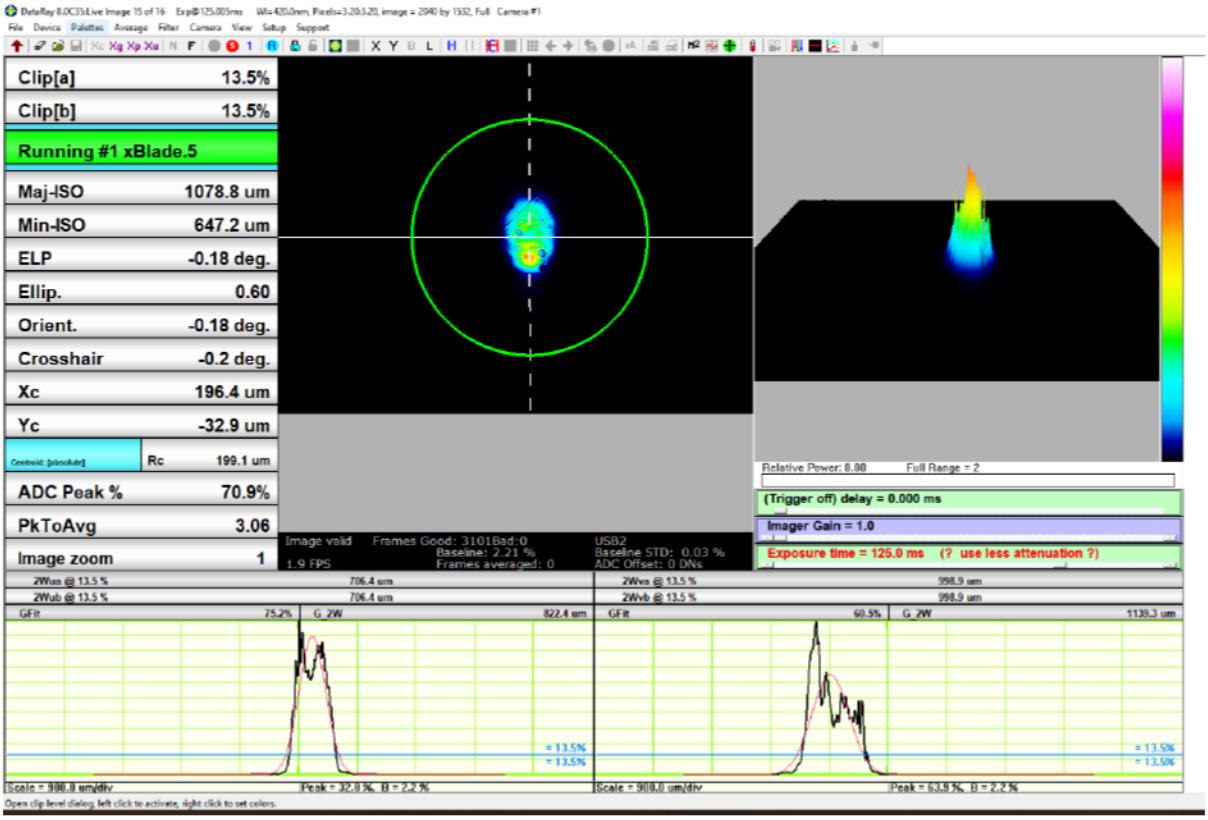

Figure 9. Output from the 420 nm laser measured with a DataRay BladeCam-XHR. For the purposes of this report, the Gaussian fit values of 706.4 μm and 998.9 μm will be used as the beam "diameters".

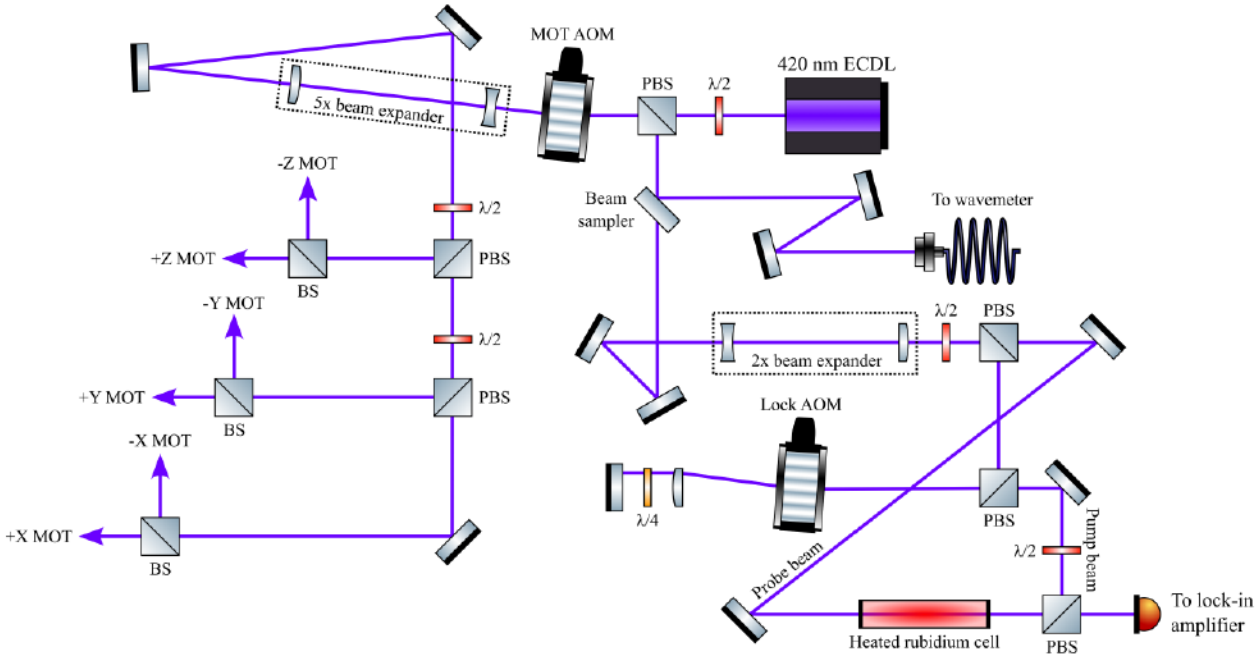

Figure 10. Schematic of the 420 nm laser system for both absolute frequency stabilization and for producing the six independent MOT beams ($+X$, $-X$, $+Y$, $-Y$, $+Z$, and $-Z$). BS: nonpolarizing 50:50 beam splitter; PBS: polarizing beam splitter; $\lambda/2$: half-waveplate; $\lambda/4$: quarter-waveplate; AOM: acousto-optic modulator. Drawn using [68].

The output from the photodetector is input to the lock-in amplifier (Stanford Research Systems SR830) from which the demodulation produces the error signals shown in Figure 16. This error signal is fed to a New Focus LB1005 that controls the 420 nm ECDL's grating tuning element to stabilize the absolute frequency. In the future, stabilizing the 420 nm laser using an EOM as in a standard MTS setup (e.g., as in [72, 73]) would likely produce a larger signal and be less susceptible to drifts (e.g., varying AOM diffraction powers).

The remaining 420 nm light not diverted for laser stabilization is single-passed through the MOT AOM to provide amplitude modulation and limited frequency tuning. This AOM is centered at about -200 MHz so the light delivered to the atoms is near the $|5S_{1/2}, F = 2\rangle \rightarrow |6P_{3/2}, F = 3\rangle$ resonance. This beam is then expanded by about $5\times$ to have approximate diameters of $3.5\text{ mm} \times 5\text{ mm}$ (note the Figure 9 caption). It should be noted that using small diameter MOT beams leads to highly unfavorable scaling of the atom number [74] so future experiments should aim to reduce transmission losses to facilitate larger MOT beams. A series of half-waveplates and polarizing beam splitters generate three MOT beams (X, Y, and Z) from which nonpolarizing 50:50 beam splitters further divide the beams into the six independent MOT beams ($+$X, $-$X, $+$Y, $-$Y, $+$Z, and $-$Z).

Combining the 780 nm and 420 nm MOT Beams

Due to the glass cell's transmission properties, we decided to implement a three beam retroreflected 780 nm MOT and a six independent beam 420 nm MOT. The three 780 nm and six 420 nm beams were combined using dichroic mirrors that reflected 420 nm and transmitted 780 nm. For the dual-wavelength quarter-waveplates to generate the same handedness circular polarization, both the 780 nm and 420 nm MOT beams must have the same incident linear polarization. A simplified sketch of the 780 nm and 420 nm MOT combining optics is shown in Figure 11 with some elements (e.g., modulators, additional mirrors) omitted for clarity.

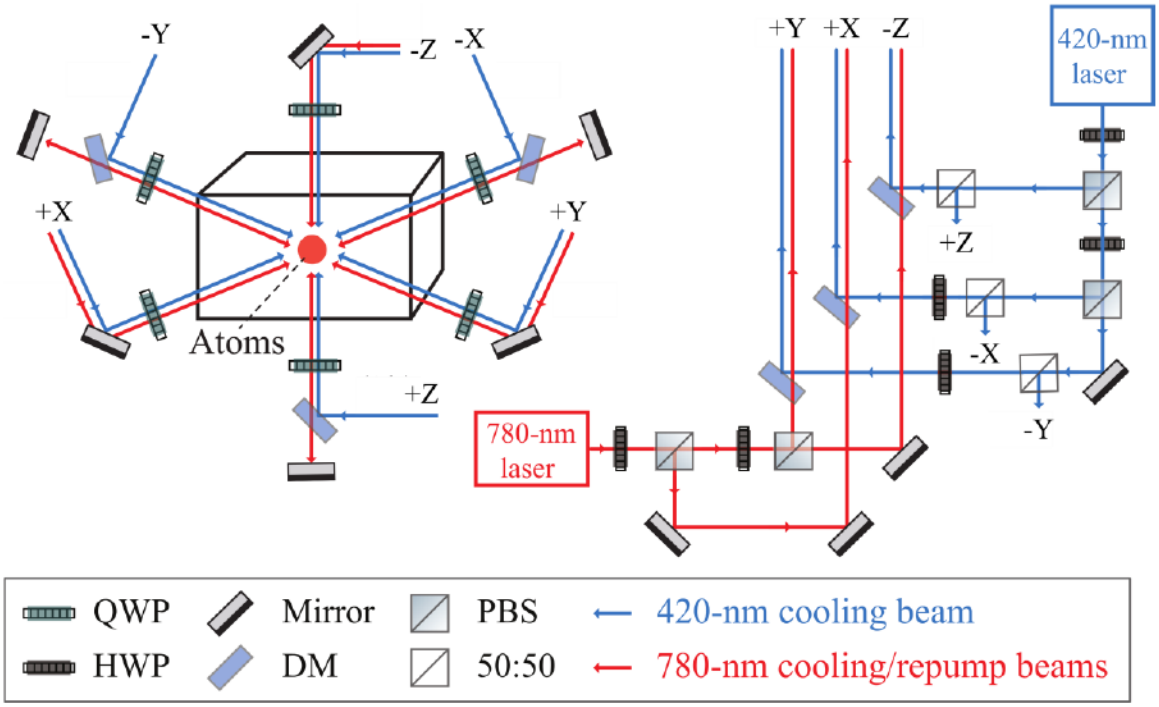

Figure 11. Simplified sketch of the optics for combining the three 780 nm retroreflected MOT beams with the six independent 420 nm MOT beams. Some elements (e.g., modulators, additional mirrors) were omitted for clarity. QWP: quarter-waveplate; HWP: half-waveplate; DM: dichroic mirror transmitting 780 nm and reflecting 420 nm; PBS: polarizing beam splitter; 50:50: nonpolarizing beam splitter with a 50:50 ratio.

Experiment Control System

The original control system was based on National Instruments (NI) analog input/output PCI cards with timing and control provided by a field-programmable gate array (FPGA) running custom code (likely similar to the system described in [75]). Although highly powerful for performing one (or a few) specific experiment(s), it lacked the flexibility needed for this and future projects where the parameter space being explored is large and not well-defined.

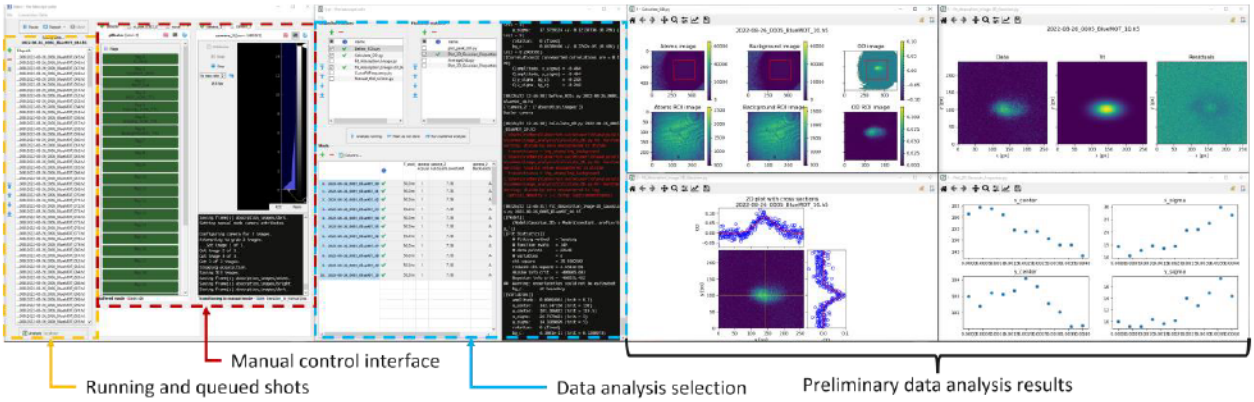

Figure 12. Example labscript suite experiment control interface while running an experiment.

Prior to this project, some work was done to migrate the system over to a commercial-off-the-shelf timing solution (SpinCore PulseBlaster) to enable some system flexibility and long-term usability. This effort was significantly advanced during this project as we implemented the Python-based labscript suite [76-78] for computer experiment control. Figure 12 shows an annotated screenshot while running an experiment.

The labscript suite combines a very flexible and extensible architecture that leverages the many types of commercially available equipment with easily readable Python scripts. Data from each experimental shot is stored in a hierarchical data format (HDF5) with much of the system parameters for future analysis or examination. Due to the Python-based nature of labscript suite, we can now use Sandia's Common Engineering Environment (CEE) GitLab to track code for running experiments and analyzing the data, facilitating documentation.

Absorption Imaging

In absorption imaging, a low-intensity ($s \ll 1$) resonant probe beam illuminates the atom cloud and a camera captures the resulting shadow where atoms have scattered light out of the imaging beam as shown in Figure 13.

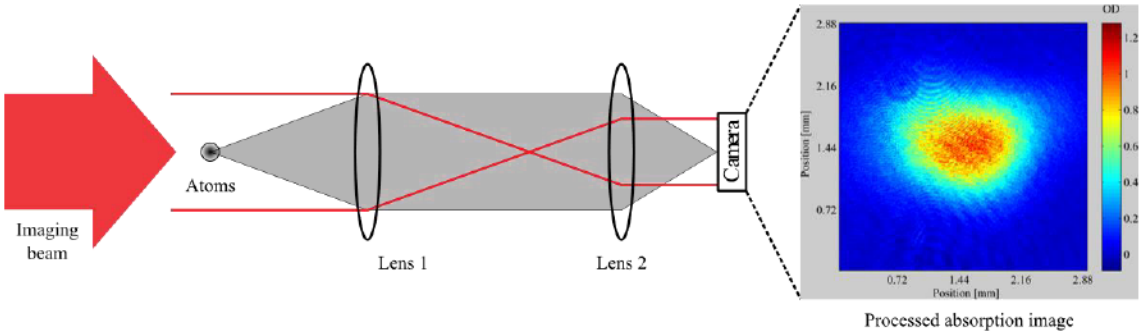

Figure 13. Example of the absorption imaging process. A low-intensity ($s \ll 1$) resonant imaging beam propagates through the atomic cloud and the resulting shadow is captured by a camera to compute the optical density (OD). Figure modified from [79].

Following [80], we capture a sequence of three images:

1. $I_{\text{atoms}}(x, y)$: pulse on imaging beam with the atoms present to capture their shadow
2. $I_{\text{bright}}(x, y)$: pulse on imaging beam after the atoms have moved out of the field-of-view to capture the intensity distribution of the imaging beam
3. $I_{\text{dark}}(x, y)$: a dark image with no imaging light (optional step)

where $I(x, y)$ represent the intensity of the imaging light detected by a pixel located at (x, y) on the sensor. From this sequence of images, the optical density (OD) can be calculated using [80]

$$\text{OD}(x, y) = \ln\left[\frac{I_{\text{bright}}(x, y) - I_{\text{dark}}(x, y)}{I_{\text{atoms}}(x, y) - I_{\text{dark}}(x, y)}\right]$$

An example of the images $I_{\text{atoms}}(x, y) - I_{\text{dark}}(x, y)$, $I_{\text{bright}}(x, y) - I_{\text{dark}}(x, y)$, and the resulting $\text{OD}(x, y)$ are shown in Figure 14. In the experiment, two imaging pulses of about 15 μs long were used as the "flashes" with the images captured on a CCD sensor (Basler acA640-120um).

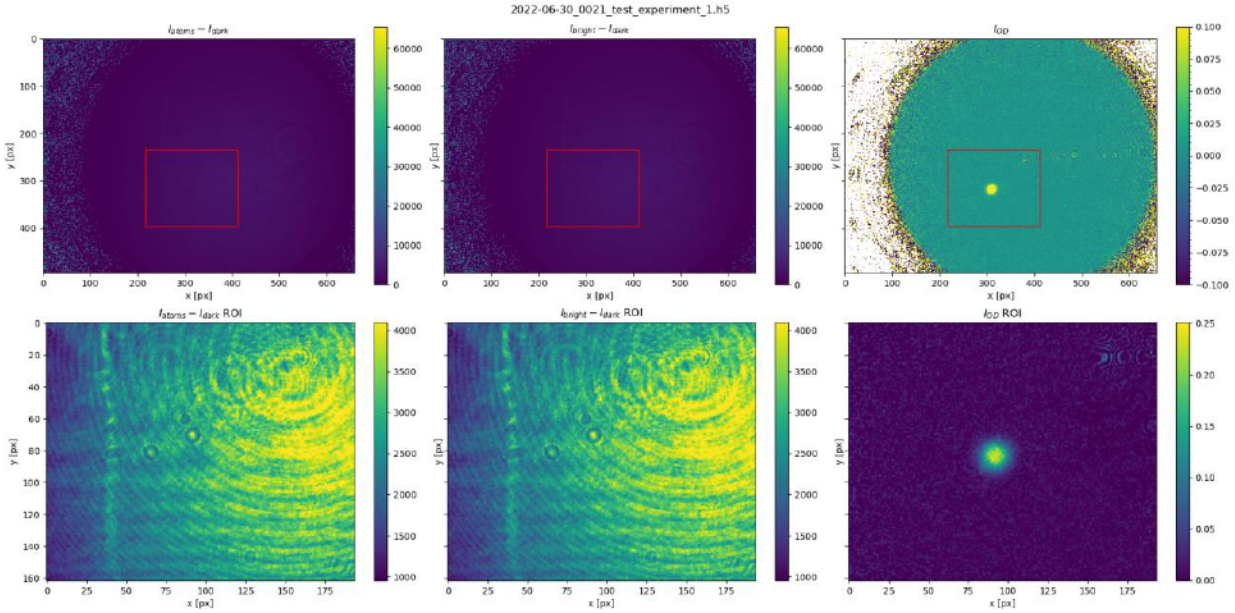

Figure 14. Example absorption imaging sequence of an expanding ^{87}Rb MOT after a 1.25 ms time-of-flight with the calculated $I_{atoms}(x,y) - I_{dark}(x,y)$ (left column), $I_{bright}(x,y) - I_{dark}(x,y)$ (middle column), and the resulting $OD(x,y)$ (right column). (Upper row) entire camera field-of-view with the red box indicating the region-of-interest (ROI). (Bottom row) showing data only from the ROI.

From $\mathrm{OD}(x,y)$, the spatial density distribution integrated along the imaging axis (the "column density" $n(x,y)$) can be extracted using

$$n(x,y) = \frac{1}{\sigma_0}\mathrm{OD}(x,y)$$

where σ_0 is the absorption cross section, which requires some additional knowledge of the imaging conditions (e.g., imaging light polarization, bias magnetic field). The total atom number (N) can be extracted by summing/integrating over all the pixels

$$N = \iint n(x,y)\,dx\,dy$$

For the purposes of this project, we were primarily interested in the spatial distribution and did not focus on extracting atom number.

Time-of-Flight (ToF) Measurement

A time-of-flight measurement is performed by extinguishing the trapping fields and allowing the previously trapped atoms to ballistically expand. This maps the initial momentum distribution of

the trapped atom cloud to a position distribution [81] that can be recorded with absorption imaging. An example of a series of time-of-flight absorption images is shown in Figure 15.

For a thermal atom cloud with an initial radius r_0, the radius expands with drop time t_{Drop} as

$$r(t_{\mathrm{Drop}}) = \sqrt{r_0^2 + \frac{k_B T}{M} t_{\mathrm{Drop}}^2}$$

where k_B is the Boltzmann constant and M is the atomic mass [79, 81]. By varying t_{Drop}, the cloud temperature (T) can be extracted by fitting the above equation.

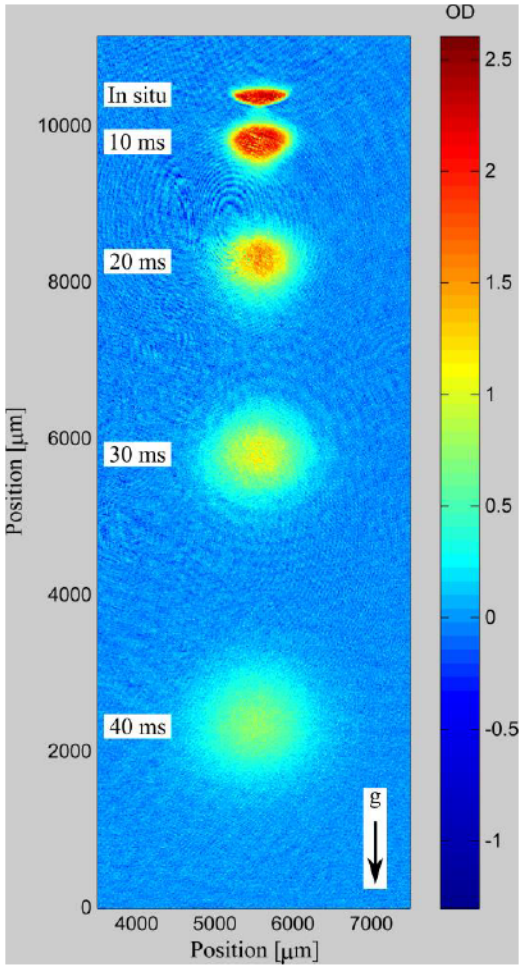

Figure 15. Example of a series of time-of-flight absorption images of a strontium 689 nm narrow linewidth MOT at approximately 1.4 μK (from [79]). The figure was chosen to show that the atom cloud both expands radially and the center-of-mass moves vertically due to gravity.

The time-of-flight method also provides an easy *in situ* method to relate the camera pixel positions to a physical distance by tracking the atomic cloud's center-of-mass as it falls under the influence of gravity (see Figure 15). The pixel size calibration using a gravity drop avoids the need to disturb the experimental setup, such as to place a USAF resolution test target at the position of the atoms. The resulting conversion factor also naturally includes the magnification factor of the imaging system.

RESULTS AND DISCUSSION:

Stabilizing the Absolute Frequency of the 420 nm Laser

The first task is the stabilization of the absolute frequency of the 420 nm ECDL to one of the ^{87}Rb $\left|5S_{1/2}, F = 2\right\rangle \rightarrow \left|6P_{3/2}, F'\right\rangle$ transitions. Due to narrow linewidth and weakness of the 420

nm transition (see Table 2), the laser needs to be stable to a fraction of the linewidth (i.e., better than about 1 MHz) to be able to produce repeatable measurements. This was achieved using the spectroscopy setup shown in Figure 10 with the demodulated error signal shown in Figure 16. Because the spectroscopy pump beam is shifted by about -400 MHz relative to the unmodulated probe beam, this causes the 420 nm ECDL to be stabilized to $+200$ MHz above the atomic resonance.

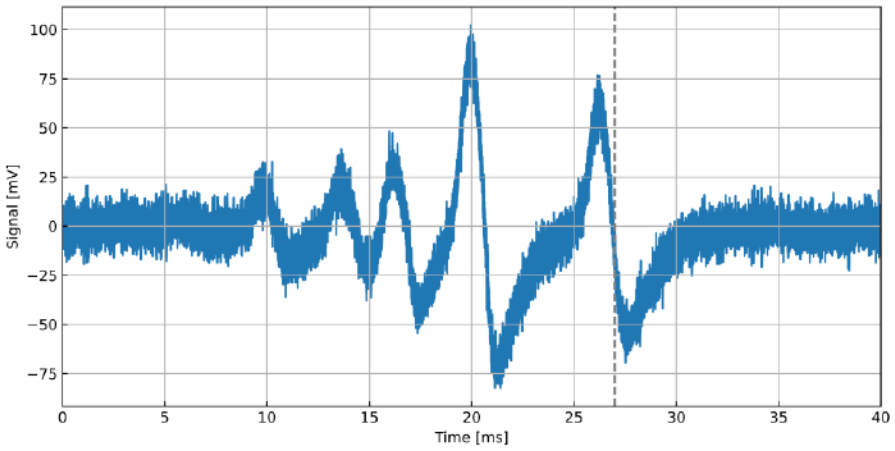

Figure 16. Demodulated 420 nm error signal from the lock-in amplifier while scanning over the ^{87}Rb $|5S_{1/2}, F = 2\rangle \rightarrow |6P_{3/2}, F'\rangle$ hyperfine lines. Dashed vertical line indicates the $|5S_{1/2}, F = 2\rangle \rightarrow |6P_{3/2}, F' = 3\rangle$ lock point.

Before proceeding further, we checked that the 420 nm laser is locked to the correct ^{87}Rb transition and that the 420 nm MOT AOM (Figure 10) at about -200 MHz provides the correct shift to be near resonance. This was accomplished by driving the MOT AOM at -204 MHz (i.e., 4 MHz lower in absolute frequency than the signals observed with the spectroscopy setup) to introduce a known frequency offset between the Lock and MOT paths. The resulting spectroscopy signals are shown in Figure 17. Upon comparison with [57], we can confirm that we are seeing the ^{87}Rb $|5S_{1/2}, F = 2\rangle \rightarrow |6P_{3/2}, F'\rangle$ hyperfine lines as the splittings line up relatively well with their expected values. The systematic discrepancy can likely be attributed to the laser tuning nonlinearly with voltage (e.g., using the current feedforward feature).

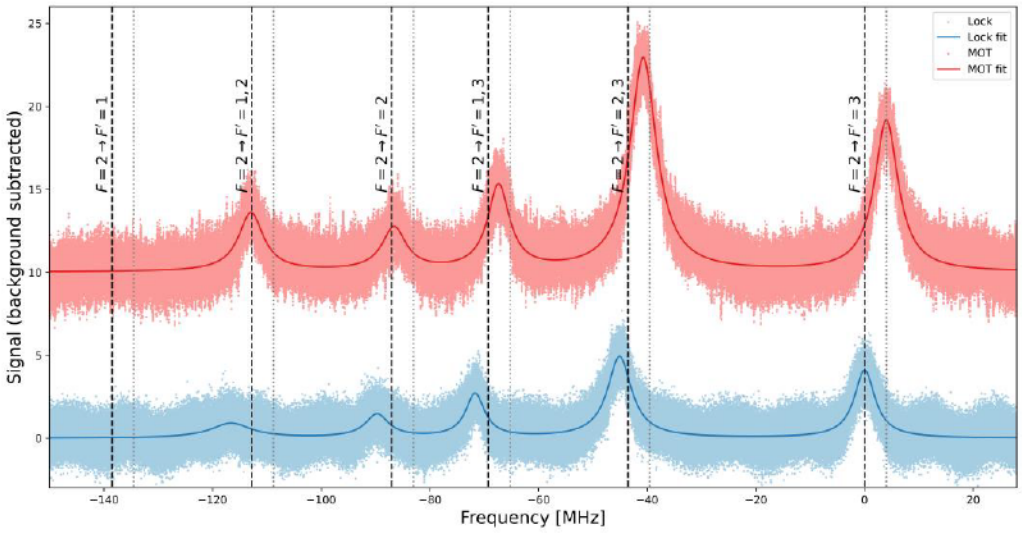

Figure 17. Comparison of 420 nm saturated absorption spectroscopy peaks from the spectroscopy path (blue) vs. the MOT path (red), vertically offset for clarity. Defining the spectroscopy path's $|5S_{1/2}, F = 2\rangle \rightarrow |6P_{3/2}, F' = 3\rangle$ peak as the origin and the 4 MHz relative shift as the calibration factor, the vertical lines indicate the expected resonance positions from [57] for the spectroscopy path signal (dark dashed) and MOT path signal (light dotted).

Although we were able to stabilize the laser well enough for our purposes, we suspect there to be some slow drifts in the lock point (e.g., varying pump powers, Lock AOM beam pointing). In the future, stabilizing the 420 nm laser using an EOM as in a standard MTS setup would likely produce a larger and more stable signal [72, 73].

Observation of a 420 nm MOT

The main goal of this project is to produce a low temperature cloud of ^{87}Rb atoms using the 420 nm transition. We begin this section by presenting the calibration of the absorption imaging scale factor to extract quantitative information from subsequent time-of-flight measurements. We then show absorption images of atoms captured by the 420 nm MOT beams (i.e., the observation of a 420 nm MOT). Lastly, we perform a time-of-flight measurement to determine the temperature of the 420 nm MOT.

Calibrating the Absorption Imaging Scale

We take absorption images of the atom cloud to determine the temperature. A Basler acA640-120um CCD camera is triggered to take images of the atom cloud as it expands due to their finite temperature. The image output is an array of pixel values and must be calibrated to get a measure of distance, i.e., a conversion from pixels to micrometers. This method involves dropping the

atom cloud and taking images at different delay times. The trajectory of the atom cloud follows the kinematic equation for an object falling due to gravity

$$y = y_0 + v_{0,y}t + \frac{1}{2}a_y t^2$$

where y_0 is the initial position of the atom cloud, $v_{0,y}$ is the initial velocity of the cloud, a_y is the cloud acceleration in the y-direction, and t is the drop time. The initial velocity of the cloud, $v_{0,y}$, has been equated to zero in the analysis below. The benefit of using this method is that no experiment component must be removed to perform the calibration. Other methods use test targets placed in front of the camera-lens system, requiring the repositioning of the camera or removal of the vacuum cell. Moving any of these components results in changes to the experiment conditions which can lead to systemic errors. Although this method is simple and straight forward to apply in practice, the temperature of the atoms could be a limiting factor. For example, in our experiment the atom temperature allowed a maximum of 5 ms of drop time before the cloud expansion reduced the optical depth to unmeasurable levels i.e., we didn't have enough signal to observe the cloud. Assuming an initial velocity of zero, this indicates the cloud dropped a maximum of 123 µm which was comparable to uncertainty of our measurements. To circumvent this issue, we applied polarization gradient cooling (PGC) [34] to extend the drop time to 20 ms allowing ~2 mm of drop distance.

The calibration experiment is as follows. We start by loading the 780 nm MOT for 10 s after which the cooling light and quadrupole field are abruptly shut off. The atom cloud is allowed to drop and expand for a drop time, *t*. After this time, the camera is triggered to take three images: an atom image, a probe image with no atoms, and a dark image with each image separated by 50 ms to allow for camera readout. First, the atom image (I_{atoms}) is taken by flashing on both the resonant repump and imaging beams for 14 µs, capturing the atom cloud shadow. Next, the probe image (I_{bright}) is taken 50 ms after the atom image, also with both the repump and probe on for the same 14 µs flash duration. In addition to allowing for camera readout of the previous image, the 50 ms delay also allows any remaining atoms to escape the imaging region or to be diluted below the noise level. Finally, the dark image (I_{dark}) is taken without any beams on to take an image of background signal. The data is shown in Figure 18 and a curve fit results in a 31.83 µm/pixel conversion factor assuming $g = 9.8\,\text{m/s}^2$.

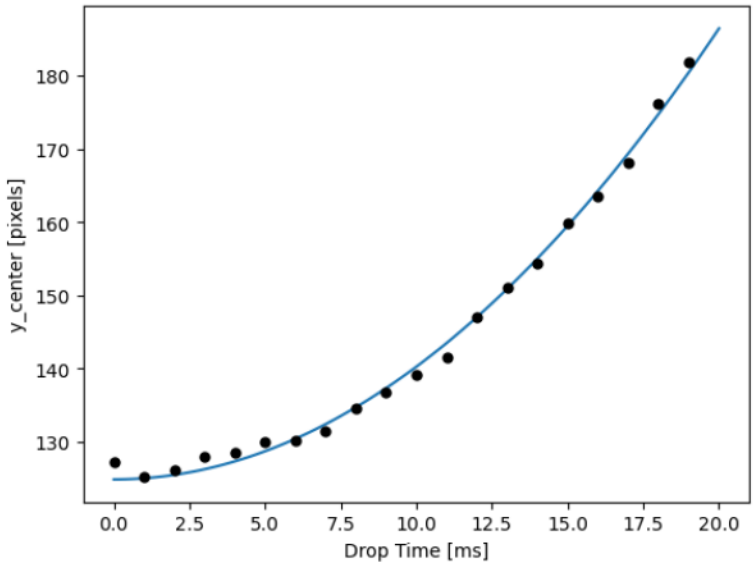

Figure 18. Atom cloud free fall data. The y-axis center-of-mass of the cloud is extracted from a 2D Gaussian fit after a variable drop time. Each data point is the one experimental shot. The resulting conversion factor is $31.83\,\mu m/pixel$ assuming $g = 9.8\,m/s^2$.

Effect of 420 nm MOT Light

Next, we study the effect of the 420 nm light on the expansion of the atom cloud after being released from the 780 nm MOT. To compare the effects with the 420 nm light on and off we run two experiments with the only variable changing is whether the 420 nm light is on or off. A timing diagram of the experiment is shown in Figure 19.

As a reference, we first study the atom cloud expansion with the 420 nm light off. We begin the experiment by loading the 780 nm MOT for 10 s after which the cooling light is abruptly shut off. The quadrupole magnetic field (B-field) and repump are kept on. A "narrow-line cooling" interval is introduced after the 780 nm cooling beams are shut off. Images of the expanding cloud are shown in Figure 20 (top row) for narrow-line cooling times between $2 - 8$ ms before absorption imaging. Without 420 nm MOT light, the atomic cloud is clearly observed to expand more than twice its original size. A quantitative measure of the atomic temperature is given in the next section.

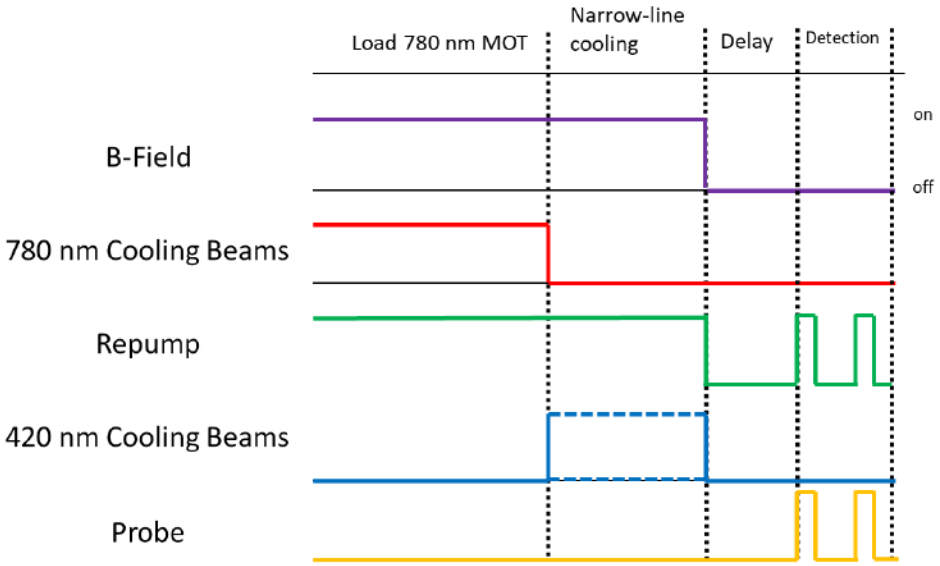

Figure 19. Schematic timing diagram for observing the atom cloud with and without the 420 nm MOT beams after the 780 nm MOT is turned off (indicated by the dashed 420 nm Cooling Beam lines).

To determine the effects of the 420 nm light on the cloud, we modify the experiment by turning on the 420 nm laser after the cooling beams are shut off for a variable time between $2 - 8$ ms during the narrow-line cooling stage (see Figure 19). The B-field and repump are kept on during the 420 nm pulse to load atoms into the 420 nm MOT. The effects of applying the 420 nm MOT light is evident in Figure 20 (bottom row) where atoms are no longer freely expanding after extinguishing the 780 nm cooling beams. In fact, the 420 nm cooling beams contain and compress the atoms released from the 780 nm MOT. We do observe a displacement between the 780 nm MOT center and the 420 nm MOT center. We believe this could be due to stray magnetic fields or the weird intensity profile of the 420 nm laser output.

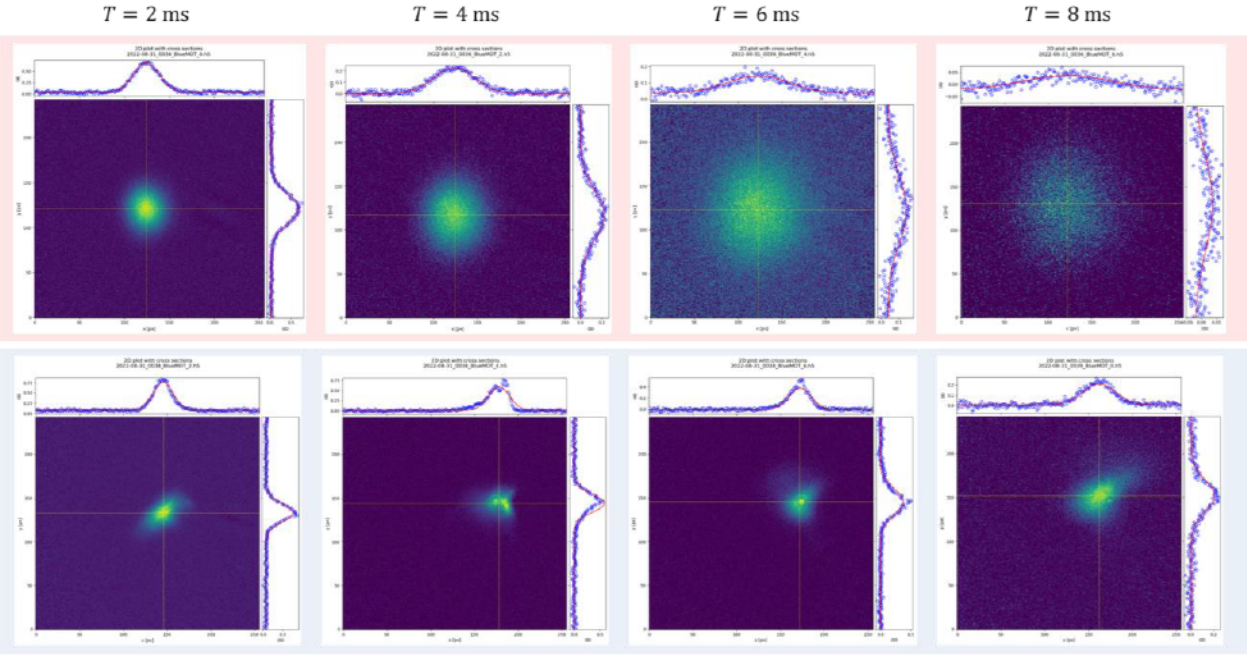

Figure 20. Absorption images showing the effects without (top row) and with (bottom row) 420 nm cooling beams after the 780 nm cooling beams are extinguished. Compared to the freely expanding atoms released from the 780 nm MOT (top row), the 420 nm MOT is clearly present.

Measurement of 420 nm MOT Temperature

The temperature of the atomic cloud is measured using a time-of-flight method for both a MOT using 780 nm light only and after loading the 420 nm MOT. The timing diagram of the experiments is the same as before and is shown in Figure 19. In the 780 MOT TOF measurements, the "narrow-line cooling time interval" is zero so that the quadrupole field and repump turn off simultaneously with the cooling beams. The 420 nm MOT is loaded after extinguishing the cooling beams for the 780 nm MOT.

In the 780 nm MOT temperature measurements, the MOT is loaded for 5 s after which the 780 nm cooling light is abruptly shut off. The atom cloud is allowed to expand for a variable drop time and fitted using a 2D Gaussian model to extract the radius. The red data points in Figure 21 show the atom cloud radius as a function of drop time for the 780 nm MOT. The radius data has two fit parameters, the radius σ_0 and temperature T. The temperature of the cloud using only 780 nm cooling light is found to be $T_x = 499$ μK and $T_y = 650$ μK. This temperature is much higher than the Doppler cooling limit of 146 μK which is typically difficult to achieve [30]. To investigate this effect, we changed the quadrupole zero point by applying a bias field and found that the temperature reduced significantly to $T_x = 193$ μK and $T_y = 207$ μK. However, the applied bias field displaced the cloud and reduced the loading efficiency of the 420 nm MOT. Unfortunately, due to equipment delays there wasn't enough time to optimize this loading

efficiency and we report the higher temperature values to compare to the temperature of the 420 nm MOT measurements which are discussed next.

To measure the temperature of the atom cloud using the 420 nm MOT, we use the same sequence as for the 780 nm MOT however, now the "narrow-line cooling" interval is used to load the 420 nm MOT as shown in Figure 19. This interval lasts 4 ms. After this loading time, all beams and the quadrupole field are shut off and the drop time is scanned. We also found that the minimum temperature is achieved with a detuning of -1.6 MHz from the $5S_{1/2} \rightarrow 6P_{3/2}$ transition and use this detuning for these experiments. The results for the 420 nm time-of-flight measurement are shown in blue in Figure 21. The temperature of the cloud using the 420 nm cooling light is $T_x = 189$ μK and $T_y = 452$ μK. We suspect the large discrepancy between the observed horizontal (T_x) and vertical (T_y) temperatures could be due to near-normal reflections off the glass cell for the vertical 420 nm MOT beams that could lead to incorrect circular polarization being incident on the atoms.

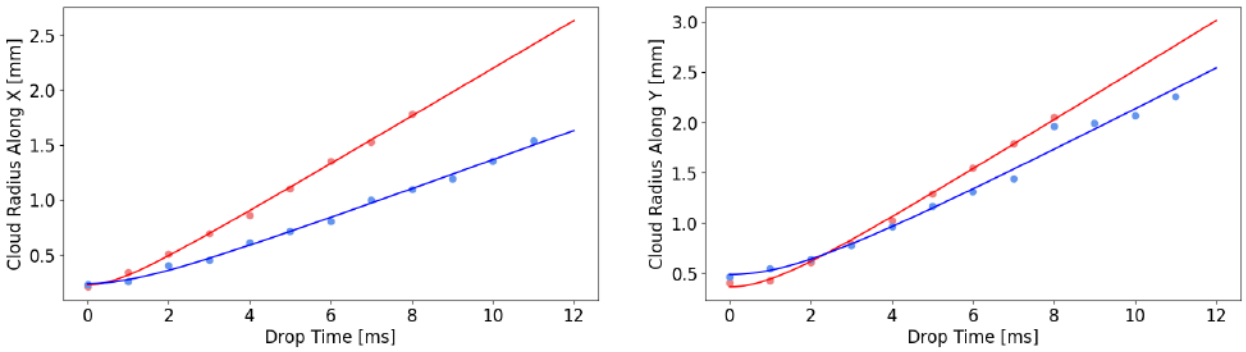

Figure 21. Time-of-flight temperature measurements of atoms released from the 780 nm MOT (red points) and after 4 ms in the 420 nm MOT (blue points). Left shows data for the horizontal (x) cloud radius and right for the vertical (y) cloud radius. Fit results give $T_{x,780\,nm} = 499\ \mu K$, $T_{x,780\,nm} = 650\ \mu K$, $T_{x,420\,nm} = 189\ \mu K$, and $T_{x,420\,nm} = 452\ \mu K$.

Although further characterization and optimization are needed to achieve lower temperatures, the initial measurements in Figure 21 clearly show that the 420 nm MOT temperature is already comparable to the Doppler cooling limit of the 780 nm MOT. In both cases, we find that the temperature in the x-direction is lower than in the y-direction. A potential factor is due to some undiffracted zeroth-order 420 nm light from the MOT AOM incident on the glass cell. This 420 nm light is far-detuned from atomic resonance but was observed to have some strange effects on the ballistically-expanding atom clouds.

In addition, we investigate the temperature of the 420 nm narrow line MOT as a function of hold time. The hold time is the time for which the atoms are held in the 420 nm MOT. As previously mentioned, the hold time for the measurements in Figure 21 was 4 ms. As shown in Figure 22,

the temperature of both the horizontal (blue dots) and vertical (orange dots) decrease as a function of hold time with a minimum observed temperature of $T_x \approx 150$ μK and $T_y \approx 250$ μK.

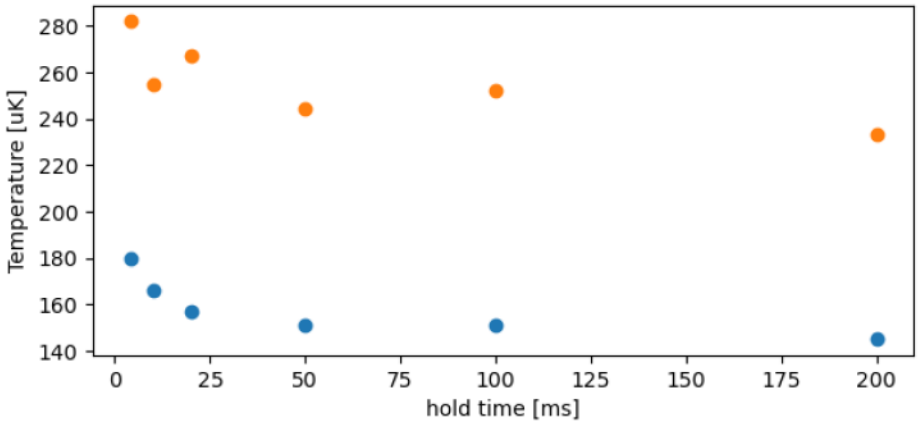

Figure 22. Temperature of the 420 nm MOT after varying hold time for the horizontal (T_x, blue dots) and vertical (T_y, orange dots) directions. In both cases, the temperature decreases as hold time is increased up to ~50 ms.

Towards a 420 nm Grating Magneto-Optical Trap (GMOT)

We also started investigating the possibility of making a 420 nm grating magneto-optical trap (GMOT). In a typical tetrahedral GMOT, a single incident cooling beam is incident on three diffraction gratings arranged in triangle, resulting in three first-order diffracted beams directed back towards the incident cooling beam [36, 82, 83]. This offers significant advantages for future sensors due offering a compact form factor while being simple for field operation. GMOTs are currently being pursued for a variety of sensing applications including atom interferometers [84], microwave clocks [85], optical clocks [86, 87], magnetic field sensing [36], and vacuum metrology [88].

Current state-of-the-art rubidium GMOTs use the well-established 780 nm transition and apply sub-Doppler cooling to achieve temperatures below the rubidium 780 nm Doppler cooling limit [36, 38]. Although effective at cooling below T_D, sub-Doppler cooling is highly susceptible to stray magnetic fields [36] and requires extinguishing the trapping fields (i.e., the atoms get colder at the expense of spatial confinement). Oddly, sub-Doppler cooling in GMOTs tends to be less efficient than in standard six-beam MOTs and often requires a longer duration [38]. A 420 nm narrow linewidth GMOT offers a straightforward path towards producing cold atomic samples while keeping the atoms trapped.

For an initial investigation towards realizing a 420 nm tetrahedral GMOT, we considered two commercial-off-the-shelf blazed gratings (see Table 4). Potential performance of the selected gratings were calculated assuming a single uniform intensity 420 nm cooling beam (i.e., the

single laser cooling beam for the GMOT) and using multilevel binary gratings in Grating Diffraction Calculator (GD-Calc) [89].

Table 4. Parameters for commercial-off-the-shelf reflective diffraction gratings considered for a tetrahedral 420 nm grating magneto-optical trap (GMOT). Both gratings have external dimensions of approximately $12.7 \times 12.7 \times 6\ mm^3$.

Manufacturer	Item	Type	Groove density [groves/mm]	Design wavelength [nm]	Blaze angle [°]	Coating
Edmund Optics	#48-464	Ruled grating	1200	400	13.88	Aluminum
Richardson Gratings (via Edmund Optics)	320H (#15-751)	Holographic grating	1800	450		Aluminum

The first grating (Edmund Optics #48-464) is designed for 400 nm and has grating periodicity $d = (1200\ \text{groves/mm})^{-1} = 833.333$ nm. We constructed a multilevel binary grating ($N = 50$) to approximate the physical grating and performed the simulation for 420 nm incident light. The results are shown in Figure 23. The second grating (Richardson Gratings 320H) has groove density $d = (1800\ \text{groves/mm})^{-1} = 555.556$ nm and designed is 450 nm. This grating was also approximated with a multilevel binary grating model ($N = 50$) and the simulation performed with 420 nm incident light. The simulation results are shown in Figure 24.

(a)

Diffraction efficiencies (m1, eff1, eff2, eff3, eff4)

R:

-1	0.70889	0.81204	0.76047	0.76047
0	0.041497	0.0015472	0.021522	0.021522
1	0.15566	0.016935	0.0863	0.0863

T:

Energy loss:

0.093948 0.16948 0.13171 0.13171

Diffraction efficiencies (with H3=0, E3=0)

R:

-1	0.70889	0.81204
0	0.041497	0.0015472
1	0.15566	0.016935

T:

Energy loss:

0.093948 0.16948

(b)

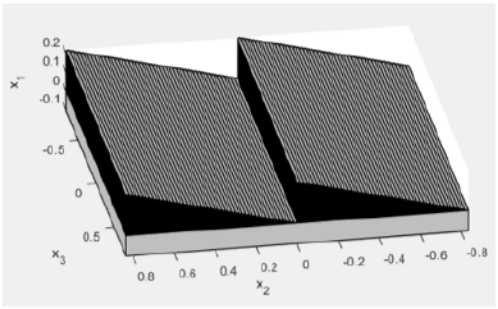

(c)

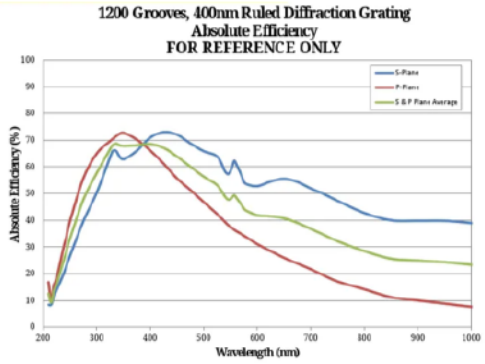

Figure 23. Simulating Edmund Optics ruled diffraction grating #48-464 (1200 grooves/mm, 400 nm target wavelength). (a) GD-Calc [89] simulation results for 420 nm incident light where reflective diffraction orders (R: m1) are -1/0/+1 and light polarization dependence (eff1: linear 1, eff2: linear 2, eff3: circular 1, eff4: circular 2). (b) Multilevel binary grating model ($N = 50$) used for the simulation. (c) Specified diffraction efficiency.

(a)

Diffraction efficiencies (m1, eff1, eff2, eff3, eff4)

R:

-1	0.60687	0.6664	0.63664	0.63664
0	0.11144	0.0057236	0.058584	0.058584
1	0.18287	0.16998	0.17642	0.17642

T:

Energy loss:

0.098816 0.1579 0.12836 0.12836

Diffraction efficiencies (with H3=0, E3=0)

R:

-1	0.60687	0.6664
0	0.11144	0.0057236
1	0.18287	0.16998

T:

Energy loss:

0.098816 0.1579

(b)

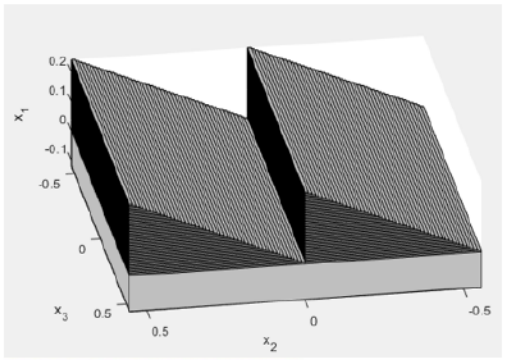

(c)

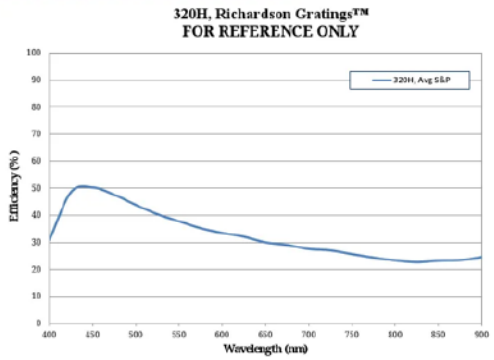

Figure 24. Simulating the plane holographic grating Richardson Gratings 320H (1800 grooves/mm, 450 nm target wavelength). (a) Simulation results from GD-Calc [89] for 420 nm incident light where reflective diffraction orders (R: m1) are -1/0/+1 and light polarization dependence (eff1: linear 1, eff2: linear 2, eff3: circular 1, eff4: circular 2). (b) Multilevel binary grating model ($N = 50$) for the simulation. (c) Specified diffraction efficiency.

In a GMOT, the intensity balance of the axial GMOT cooling beams (along the direction of the incident cooling beam) needs to be carefully considered. In a tetrahedral GMOT with a single incident cooling beam and three first-order diffracted beams, each diffracted beam should contribute approximately $1/3$ of the axial scattering force to balance the incident cooling beam. For a uniform intensity (i.e., flat-top) incident cooling beam, this means each diffracted beam should contribute about $1/3$ of the incident intensity along this axis.

For the first grating (Edmund Optics #48-464), a normally incident 420 nm beam leads to the first order diffraction angle of $\theta_1 = 30.265°$. Assuming a flat-top incident cooling beam, each diffracted beam provides approximately $\cos(\theta_1) \times [\text{diffraction efficiency}] = 0.8637 \times 0.76047 \approx 0.657$ of the incident scattering force. For gratings located inside the glass cell, this value is larger than $1/3$ meaning an imbalance in the axial scattering force would likely result. If the gratings are located outside the glass cell (non-AR-coated for 420 nm), only $\approx 58\%$ of the intensity will be returned (exiting the glass cell, diffracting off the gratings, and then reentering the glass cell). Therefore, each diffracted beam would provide about 0.384 of the incident beam scattering force. Since this is close to $1/3$, a GMOT could potentially form.

Again, assuming the same uniform intensity incident 420 nm beam for the second grating (Richardson Gratings 320H), the first order diffraction angle is $\theta_1 = 49.11°$. Hence, the scattering provided by each diffracted beam along the axis is approximately $\cos(\theta_1) \times$ [diffraction efficiency] $= 0.6546 \times 0.63664 \approx 0.417$ of the incident beam. Again, this value is a bit large if the gratings are located inside the glass cell. If the gratings are located outside the glass cell, the $T \approx 58\%$ two-way transmission leads to each diffracted beams containing about 0.244 of the incident intensity, meaning the axial scattering force is also likely to be imbalanced with this grating.

From the results above, externally mounted Edmund Optics #48-464 gratings seem like the most promising commercially available candidate for producing a GMOT. It should be noted however that larger diffraction angles tend to contribute more transverse scattering force (i.e., stronger confinement perpendicular to the incident beam axis). The steeper diffraction angle also results in an increase of the diffracted intensity due to beam "compression", meaning that the Richardson Gratings 320H should also be tested for GMOT operation. Of course, having appropriate AR-coatings for 780 nm and 420 nm would significantly alleviate design constraints.

The realization of a 420 nm GMOT will leverage Sandia expertise in microfabricated grating chips for 780 nm (aluminum deposition after e-beam lithography) [84] and will accelerate the development of grating chips at 420 nm. We can also follow the two-color (dual-wavelength) GMOT approach as demonstrated for strontium (461 nm and 689 nm) [87] to develop a 780 nm and 420 nm GMOT that combines the unique advantages of those wavelengths.

Discussion

We have achieved our main key goals:

- Stabilizing the absolute frequency of the 420 nm laser to the ^{87}Rb $|5S_{1/2}, F = 2\rangle \rightarrow |6P_{3/2}, F' = 3\rangle$ transition
- Observe laser cooling and trapping of ^{87}Rb using the 420 nm transition (i.e., a 420 nm MOT)

and were very close to achieving our third goal of

- Demonstrate that the 420 nm MOT temperature is below the standard 780 nm Doppler cooling limit

Although our results are very preliminary, we have shown that narrow linewidth laser cooling of ^{87}Rb on the 420 nm $5S_{1/2} \rightarrow 6P_{3/2}$ transition is a viable path towards producing cold atoms below the standard 780 nm Doppler cooling limit. Currently, we have observed 420 nm laser cooling and trapping (i.e., a 420 nm MOT) that results in in an asymmetric temperature distribution ($T_x \approx 150$ μK $\times$ $T_y \approx 250$ μK) but this is before the opportunity to perform

characterization and optimization. With further characterization and optimization, we believe a 3D temperature below 50 μK [55] should be easily achievable.

ANTICIPATED OUTCOMES AND IMPACTS:

Having demonstrated the proof-of-concept narrow linewidth laser cooling of ^{87}Rb using the 420 nm transition, there are multiple possible future directions. Unfortunately, no publications are currently planned due to the Das et al., arXiv preprint [55] that presented results of an extremely similar experiment to ours.

Although no publications are currently planned, the work accomplished during this LDRD directly enables upcoming work in FY23 and beyond. The 780 nm laser system revived for this work will be used as the primary 780 nm laser system for exploring advanced multi-axis atom interferometry for inertial sensing. Perhaps the most significant legacy of this project was upgrading the control system from a field programmable gate array (FPGA) running custom, highly specific operations to the Python-based labscript suite [76-78]. The flexibility of the labscript suite enables rapid reconfiguration of the experimental sequences for exploration of complex and relatively unknown parameter spaces. Most importantly, labscript suite facilitates documentation of both experiment control code using Sandia's Common Engineering Environment (CEE) GitLab and data archival via the hierarchical data format (HDF5).

The most straightforward next step would be to optimize and refine the demonstrated standard six beam 420 nm MOT to better understand the parameter space. For example, we think some rudimentary optimization could easily reduce the observed ≈ 200 μK horizontal temperature and an appropriately anti-reflection coated glass cell could reduce the vertical temperature. Another remaining question is why we did not observe direct trapping from the background vapor, requiring us to use the 780 nm MOT to precool atoms for the 420 nm MOT as a mitigation. A narrow linewidth MOT of neutral ytterbium, which has a narrower laser cooling transition linewidth (556 nm with $\Gamma_{556\,\mathrm{nm}} = 2\pi(184\ \mathrm{kHz})$) than rubidium explored in this work (see Table 2), can be directly loaded from a vapor [46, 90]. A second stage narrow linewidth MOT could facilitate loading of atoms on to nano/microfabricated devices (e.g., [91-93]) and the ability to bypass the 780 nm cooling stage would be of significant benefit for future fieldable sensors, enabling the elimination of the 780 nm laser system.

Another straightforward extension of the current work is the development of a 420 nm grating magneto optical trap (GMOT). Due to its simplicity and compact form factor, it has the potential to enable future fieldable quantum sensors and Sandia has already invested in the 780 nm ^{87}Rb GMOT platform [84]. Development of a 420 nm GMOT directly leverages that experience and Sandia's unique fabrication capability. As an example, one particular avenue could be the development of a dual-wavelength ^{87}Rb GMOT (780 nm and 420 nm), similar to one demonstrated for strontium (461 nm and 689 nm) [87].

We can also have significant impact for future avenues to advance atom interferometry for measuring accelerations. In a light-pulse atom interferometer (LPAI), two coherent light fields drive coherent oscillations between the $|5S_{1/2}, F = 1\rangle$ and $|5S_{1/2}, F = 2\rangle$ hyperfine ground states. Following a $\frac{\pi}{2} \rightarrow T \rightarrow \pi \rightarrow T \rightarrow \frac{\pi}{2}$ pulse sequence, the resulting atomic population interference fringe is sensitive to acceleration according to $\sigma_a = \frac{\delta\phi}{ak_{\text{eff}}}\frac{1}{T^2}$ where $k_{\text{eff}} = k_{\text{Raman 1}} - k_{\text{Raman 2}} \approx 2k$ [40]. For a standard ^{87}Rb LPAI, the coherent oscillations are driven by two 780 nm photons with $k_{\text{eff}} = 2(2\pi/780\text{ nm})$. Replacing the 780 nm photons with 420 nm would nearly double the acceleration sensitivity for the same T since $k_{\text{eff}} = 2(2\pi/420\text{ nm}) \approx 1.86(2)(2\pi/780\text{ nm})$. Driving Raman transitions also relaxes the absolute frequency stabilization requirements of the 420 nm laser. However, if 420 nm light is used for both laser cooling and Raman pulse interrogation, the total power requirement for the laser is increased, or separate 420 nm cooling and Raman lasers might be necessary.

CONCLUSION:

We have achieved our primary goal of demonstrating laser cooling and trapping of ^{87}Rb using the narrow linewidth $5S_{1/2} \rightarrow 6P_{3/2}$ transition at 420 nm (i.e., a 420 nm MOT). The observed temperature of atoms released from the 420 nm MOT is already approaching the Doppler cooling limit using the standard $5S_{1/2} \rightarrow 5P_{3/2}$ transition at 780 nm. Although there is still much to do to explore the parameter space and optimize the 420 nm MOT (e.g., reducing the 420 nm MOT vertical temperature), the current LDRD results already open future avenues of investigation such as a 420 nm GMOT or increasing atom interferometer sensitivity. In addition, attainment of the 420 nm MOT required significant effort in reviving and upgrading existing systems that will directly benefit upcoming projects. This LDRD project also provided workforce development opportunities in the area of atomic physics (quantum sensing).

ACKNOWLEDGEMENTS:

R. Ding would like to thank Shanalyn A. Kemme (SNL) and Rick Muller (SNL) for valuable feedback and suggestions during the proposal stage.

We would also like to thank Daniel S. Barker (NIST) and Christopher Billington (University of Melbourne) for help with labscript.

REFERENCES:

[1] G. W. Hoth, B. Pelle, S. Riedl, J. Kitching, and E. A. Donley, "Point source atom interferometry with a cloud of finite size," *Applied Physics Letters,* vol. 109, no. 7, p. 071113, 2016/08/15 2016, doi: 10.1063/1.4961527.

[2] C. L. Garrido Alzar, "Compact chip-scale guided cold atom gyrometers for inertial navigation: Enabling technologies and design study," *AVS Quantum Science,* vol. 1, no. 1, p. 014702, 2019/12/01 2019, doi: 10.1116/1.5120348.

[3] K. Bongs *et al.*, "Taking atom interferometric quantum sensors from the laboratory to real-world applications," *Nature Reviews Physics,* vol. 1, no. 12, pp. 731-739, 2019/12/01 2019, doi: 10.1038/s42254-019-0117-4.

[4] F. A. Narducci, A. T. Black, and J. H. Burke, "Advances toward fieldable atom interferometers," *Advances in Physics: X,* vol. 7, no. 1, p. 1946426, 2022/12/31 2022, doi: 10.1080/23746149.2021.1946426.

[5] R. Geiger, A. Landragin, S. Merlet, and F. Pereira Dos Santos, "High-accuracy inertial measurements with cold-atom sensors," *AVS Quantum Science,* vol. 2, no. 2, p. 024702, 2020/06/01 2020, doi: 10.1116/5.0009093.

[6] M. Takamoto *et al.*, "Test of general relativity by a pair of transportable optical lattice clocks," *Nature Photonics,* vol. 14, no. 7, pp. 411-415, 2020/07/01 2020, doi: 10.1038/s41566-020-0619-8.

[7] M. Takamoto, Y. Tanaka, and H. Katori, "A perspective on the future of transportable optical lattice clocks," *Applied Physics Letters,* vol. 120, no. 14, p. 140502, 2022/04/04 2022, doi: 10.1063/5.0087894.

[8] J. Grotti *et al.*, "Geodesy and metrology with a transportable optical clock," *Nature Physics,* vol. 14, no. 5, pp. 437-441, 2018/05/01 2018, doi: 10.1038/s41567-017-0042-3.

[9] S. Origlia *et al.*, "Towards an optical clock for space: Compact, high-performance optical lattice clock based on bosonic atoms," *Physical Review A,* vol. 98, no. 5, p. 053443, 11/29/ 2018, doi: 10.1103/PhysRevA.98.053443.

[10] H. Bernien *et al.*, "Probing many-body dynamics on a 51-atom quantum simulator," *Nature,* vol. 551, no. 7682, pp. 579-584, 2017/11/01 2017, doi: 10.1038/nature24622.

[11] Y. Y. Jau, A. M. Hankin, T. Keating, I. H. Deutsch, and G. W. Biedermann, "Entangling atomic spins with a Rydberg-dressed spin-flip blockade," *Nature Physics,* vol. 12, no. 1, pp. 71-74, 2016/01/01 2016, doi: 10.1038/nphys3487.

[12] P. Scholl *et al.*, "Quantum simulation of 2D antiferromagnets with hundreds of Rydberg atoms," *Nature,* vol. 595, no. 7866, pp. 233-238, 2021/07/01 2021, doi: 10.1038/s41586-021-03585-1.

[13] K. Singh, S. Anand, A. Pocklington, J. T. Kemp, and H. Bernien, "Dual-Element, Two-Dimensional Atom Array with Continuous-Mode Operation," *Physical Review X,* vol. 12, no. 1, p. 011040, 03/02/ 2022, doi: 10.1103/PhysRevX.12.011040.

[14] C. Sheng *et al.*, "Defect-Free Arbitrary-Geometry Assembly of Mixed-Species Atom Arrays," *Physical Review Letters,* vol. 128, no. 8, p. 083202, 02/24/ 2022, doi: 10.1103/PhysRevLett.128.083202.

[15] A. Jenkins, J. W. Lis, A. Senoo, W. F. McGrew, and A. M. Kaufman, "Ytterbium Nuclear-Spin Qubits in an Optical Tweezer Array," *Physical Review X,* vol. 12, no. 2, p. 021027, 05/03/ 2022, doi: 10.1103/PhysRevX.12.021027.

[16] S. Ma, A. P. Burgers, G. Liu, J. Wilson, B. Zhang, and J. D. Thompson, "Universal Gate Operations on Nuclear Spin Qubits in an Optical Tweezer Array of $^{171}\mathrm{Yb}$ Atoms," *Physical Review X,* vol. 12, no. 2, p. 021028, 05/03/ 2022, doi: 10.1103/PhysRevX.12.021028.

[17] I. S. Madjarov *et al.*, "High-fidelity entanglement and detection of alkaline-earth Rydberg atoms," *Nature Physics,* vol. 16, no. 8, pp. 857-861, 2020/08/01 2020, doi: 10.1038/s41567-020-0903-z.

[18] B. Stray *et al.*, "Quantum sensing for gravity cartography," *Nature,* vol. 602, no. 7898, pp. 590-594, 2022/02/01 2022, doi: 10.1038/s41586-021-04315-3.

[19] X. Wu *et al.*, "Gravity surveys using a mobile atom interferometer," *Science Advances,* vol. 5, no. 9, p. eaax0800, doi: 10.1126/sciadv.aax0800.

[20] Y. Bidel *et al.*, "Absolute marine gravimetry with matter-wave interferometry," *Nature Communications,* vol. 9, no. 1, p. 627, 2018/02/12 2018, doi: 10.1038/s41467-018-03040-2.

[21] L. Earl *et al.*, "Demonstration of a Compact Magneto-Optical Trap on an Unstaffed Aerial Vehicle," *Atoms,* vol. 10, no. 1, 2022, doi: 10.3390/atoms10010032.

[22] R. Geiger *et al.*, "Detecting inertial effects with airborne matter-wave interferometry," *Nature Communications,* vol. 2, no. 1, p. 474, 2011/09/20 2011, doi: 10.1038/ncomms1479.

[23] B. Barrett *et al.*, "Dual matter-wave inertial sensors in weightlessness," *Nature Communications,* vol. 7, no. 1, p. 13786, 2016/12/12 2016, doi: 10.1038/ncomms13786.

[24] Y. Bidel *et al.*, "Absolute airborne gravimetry with a cold atom sensor," *Journal of Geodesy,* vol. 94, no. 2, p. 20, 2020/01/31 2020, doi: 10.1007/s00190-020-01350-2.

[25] D. Becker *et al.*, "Space-borne Bose-Einstein condensation for precision interferometry," *Nature,* vol. 562, no. 7727, pp. 391-395, 2018/10/01 2018, doi: 10.1038/s41586-018-0605-1.

[26] D. C. Aveline *et al.*, "Observation of Bose-Einstein condensates in an Earth-orbiting research lab," *Nature,* vol. 582, no. 7811, pp. 193-197, 2020/06/01 2020, doi: 10.1038/s41586-020-2346-1.

[27] R. Karcher, A. Imanaliev, S. Merlet, and F. P. D. Santos, "Improving the accuracy of atom interferometers with ultracold sources," *New Journal of Physics,* vol. 20, no. 11, p. 113041, 2018/11/28 2018, doi: 10.1088/1367-2630/aaf07d.

[28] P. D. Lett, W. D. Phillips, S. L. Rolston, C. E. Tanner, R. N. Watts, and C. I. Westbrook, "Optical molasses," *J. Opt. Soc. Am. B,* vol. 6, no. 11, pp. 2084-2107, 1989/11/01 1989, doi: 10.1364/JOSAB.6.002084.

[29] C. J. Foot, *Atomic Physics* (Oxford Master Series in Physics). 2005.

[30] R. Chang *et al.*, "Three-dimensional laser cooling at the Doppler limit," *Physical Review A,* vol. 90, no. 6, p. 063407, 12/01/ 2014, doi: 10.1103/PhysRevA.90.063407.

[31] R. F. Gutterres, C. Amiot, A. Fioretti, C. Gabbanini, M. Mazzoni, and O. Dulieu, "Determination of the ^{87}Rb 5*p* state dipole matrix element and radiative lifetime from the

photoassociation spectroscopy of the Rb_2 0_g^- ($P_{3/2}$) long-range state," *Physical Review A,* vol. 66, no. 2, p. 024502, 08/14/ 2002, doi: 10.1103/PhysRevA.66.024502.

[32] D. A. Steck, "Rubidium 87 D Line Data," University of Oregon, 2021. [Online]. Available: https://steck.us/alkalidata/rubidium87numbers.pdf

[33] P. D. Lett, R. N. Watts, C. I. Westbrook, W. D. Phillips, P. L. Gould, and H. J. Metcalf, "Observation of Atoms Laser Cooled below the Doppler Limit," *Physical Review Letters,* vol. 61, no. 2, pp. 169-172, 07/11/ 1988, doi: 10.1103/PhysRevLett.61.169.

[34] J. Dalibard and C. Cohen-Tannoudji, "Laser cooling below the Doppler limit by polarization gradients: simple theoretical models," *J. Opt. Soc. Am. B,* vol. 6, no. 11, pp. 2023-2045, 1989/11/01 1989, doi: 10.1364/JOSAB.6.002023.

[35] S. Rosi *et al.*, "Λ-enhanced grey molasses on the D_2 transition of Rubidium-87 atoms," *Scientific Reports,* vol. 8, no. 1, p. 1301, 2018/01/22 2018, doi: 10.1038/s41598-018-19814-z.

[36] J. P. McGilligan, P. F. Griffin, R. Elvin, S. J. Ingleby, E. Riis, and A. S. Arnold, "Grating chips for quantum technologies," *Scientific Reports,* vol. 7, no. 1, p. 384, 2017/03/24 2017, doi: 10.1038/s41598-017-00254-0.

[37] D. M. Farkas, E. A. Salim, and J. Ramirez-Serrano, "Production of Rubidium Bose-Einstein Condensates at a 1 Hz Rate," *arXiv,* vol. 1403, no. 4641, 12/24 2014, doi: 10.48550/arXiv.1403.4641.

[38] J. Lee, J. A. Grover, L. A. Orozco, and S. L. Rolston, "Sub-Doppler cooling of neutral atoms in a grating magneto-optical trap," *J. Opt. Soc. Am. B,* vol. 30, no. 11, pp. 2869-2874, 2013/11/01 2013, doi: 10.1364/JOSAB.30.002869.

[39] G. A. Phelps *et al.*, "Sub-second production of a quantum degenerate gas," *arXiv,* vol. 2007, no. 10807, 2020, doi: 10.48550/arXiv.2007.10807.

[40] H. J. McGuinness, A. V. Rakholia, and G. W. Biedermann, "High data-rate atom interferometer for measuring acceleration," *Applied Physics Letters,* vol. 100, no. 1, p. 011106, 2012/01/02 2012, doi: 10.1063/1.3673845.

[41] A. V. Rakholia, H. J. McGuinness, and G. W. Biedermann, "Dual-Axis High-Data-Rate Atom Interferometer via Cold Ensemble Exchange," *Physical Review Applied,* vol. 2, no. 5, p. 054012, 11/24/ 2014, doi: 10.1103/PhysRevApplied.2.054012.

[42] J. Lee *et al.*, "A Compact Cold-Atom Interferometer with a High Data-Rate Grating Magneto-Optical Trap and a Photonic-Integrated-Circuit-Compatible Laser System," *arXiv,* vol. 2107, no. 04792, 01/29 2022. [Online]. Available: https://arxiv.org/abs/2107.04792.

[43] E. A. Curtis, C. W. Oates, and L. Hollberg, "Quenched narrow-line second- and third-stage laser cooling of ^{40}Ca," *J. Opt. Soc. Am. B,* vol. 20, no. 5, pp. 977-984, 2003/05/01 2003, doi: 10.1364/JOSAB.20.000977.

[44] U. Sterr, T. Binnewies, C. Degenhardt, G. Wilpers, J. Helmcke, and F. Riehle, "Prospects of Doppler cooling on forbidden lines," *J. Opt. Soc. Am. B,* vol. 20, no. 5, pp. 985-993, 2003/05/01 2003, doi: 10.1364/JOSAB.20.000985.

[45] T. H. Loftus, T. Ido, M. M. Boyd, A. D. Ludlow, and J. Ye, "Narrow line cooling and momentum-space crystals," *Physical Review A,* vol. 70, no. 6, p. 063413, 12/28/ 2004, doi: 10.1103/PhysRevA.70.063413.

[46] A. Guttridge *et al.*, "Direct loading of a large Yb MOT on the $^1S_0 \rightarrow {}^3P_1$ transition," *Journal of Physics B: Atomic, Molecular and Optical Physics,* vol. 49, no. 14, p. 145006, 2016/06/28 2016, doi: 10.1088/0953-4075/49/14/145006.

[47] A. Yamaguchi, M. S. Safronova, K. Gibble, and H. Katori, "Narrow-line Cooling and Determination of the Magic Wavelength of Cd," *Physical Review Letters,* vol. 123, no. 11, p. 113201, 09/13/ 2019, doi: 10.1103/PhysRevLett.123.113201.

[48] A. Frisch *et al.*, "Narrow-line magneto-optical trap for erbium," *Physical Review A,* vol. 85, no. 5, p. 051401, 05/07/ 2012, doi: 10.1103/PhysRevA.85.051401.

[49] T. Maier, H. Kadau, M. Schmitt, A. Griesmaier, and T. Pfau, "Narrow-line magneto-optical trap for dysprosium atoms," *Opt. Lett.,* vol. 39, no. 11, pp. 3138-3141, 2014/06/01 2014, doi: 10.1364/OL.39.003138.

[50] D. D. Sukachev *et al.*, "Secondary laser cooling and capturing of thulium atoms in traps," *Quantum Electronics,* vol. 44, no. 6, pp. 515-520, 2014/06/30 2014, doi: 10.1070/qe2014v044n06abeh015392.

[51] P. M. Duarte *et al.*, "All-optical production of a lithium quantum gas using narrow-line laser cooling," *Physical Review A,* vol. 84, no. 6, p. 061406, 12/21/ 2011, doi: 10.1103/PhysRevA.84.061406.

[52] J. Sebastian, C. Gross, K. Li, H. C. J. Gan, W. Li, and K. Dieckmann, "Two-stage magneto-optical trapping and narrow-line cooling of ^{6}Li atoms to high phase-space density," *Physical Review A,* vol. 90, no. 3, p. 033417, 09/15/ 2014, doi: 10.1103/PhysRevA.90.033417.

[53] H.-Z. Chen *et al.*, "Narrow-linewidth cooling of ^{6}Li atoms using the 2S-3P transition," *Applied Physics B,* vol. 122, no. 11, p. 281, 2016/11/04 2016, doi: 10.1007/s00340-016-6556-z.

[54] D. C. McKay, D. Jervis, D. J. Fine, J. W. Simpson-Porco, G. J. A. Edge, and J. H. Thywissen, "Low-temperature high-density magneto-optical trapping of potassium using the open 4*S*→5*P* transition at 405 nm," *Physical Review A,* vol. 84, no. 6, p. 063420, 12/21/ 2011, doi: 10.1103/PhysRevA.84.063420.

[55] R. C. Das, A. B. Dangka Shylla, and K. Pandey, "Narrow-line cooling of ^{87}Rb using $5S_{1/2} \rightarrow 6P_{3/2}$ open transition at 420 nm," *arXiv,* vol. 2205, no. 04054, 2022, doi: 10.48550/arXiv.2205.04054.

[56] M. S. Safronova, C. J. Williams, and C. W. Clark, "Relativistic many-body calculations of electric-dipole matrix elements, lifetimes, and polarizabilities in rubidium," *Physical Review A,* vol. 69, no. 2, p. 022509, 02/27/ 2004, doi: 10.1103/PhysRevA.69.022509.

[57] C. Glaser *et al.*, "Absolute frequency measurement of rubidium 5*S*-6*P* transitions," *Physical Review A,* vol. 102, no. 1, p. 012804, 07/07/ 2020, doi: 10.1103/PhysRevA.102.012804.

[58] J. Marek and P. Munster, "Radiative lifetimes of excited states of rubidium up to quantum number n=12," *Journal of Physics B: Atomic and Molecular Physics,* vol. 13, no. 9, pp. 1731-1741, 1980/05/14 1980, doi: 10.1088/0022-3700/13/9/008.

[59] M. S. Safronova and U. I. Safronova, "Critically evaluated theoretical energies, lifetimes, hyperfine constants, and multipole polarizabilities in ^{87}Rb," *Physical Review A,* vol. 83, no. 5, p. 052508, 05/18/ 2011, doi: 10.1103/PhysRevA.83.052508.

[60] O. S. Heavens, "Radiative Transition Probabilities of the Lower Excited States of the Alkali Metals," *J. Opt. Soc. Am.,* vol. 51, no. 10, pp. 1058-1061, 1961/10/01 1961, doi: 10.1364/JOSA.51.001058.

[61] T. Walker, D. Sesko, and C. Wieman, "Collective behavior of optically trapped neutral atoms," *Physical Review Letters,* vol. 64, no. 4, pp. 408-411, 01/22/ 1990, doi: 10.1103/PhysRevLett.64.408.

[62] E. L. Raab, M. Prentiss, A. Cable, S. Chu, and D. E. Pritchard, "Trapping of Neutral Sodium Atoms with Radiation Pressure," *Physical Review Letters,* vol. 59, no. 23, pp. 2631-2634, 12/07/ 1987, doi: 10.1103/PhysRevLett.59.2631.

[63] H. J. Metcalf and P. v. d. Straten, *Laser Cooling and Trapping* (Graduate Texts in Contemporary Physics). Springer, 1999.

[64] S. Stellmer, "Degenerate quantum gases of strontium," Ph.D., University of Innsbruck, 2012.

[65] H. Metcalf, "Magneto-optical trapping and its application to helium metastables," *J. Opt. Soc. Am. B,* vol. 6, no. 11, pp. 2206-2210, 1989/11/01 1989, doi: 10.1364/JOSAB.6.002206.

[66] S. Eckel, D. S. Barker, E. B. Norrgard, and J. Scherschligt, "PyLCP: A Python package for computing laser cooling physics," *Computer Physics Communications,* vol. 270, p. 108166, 2022/01/01/ 2022, doi: https://doi.org/10.1016/j.cpc.2021.108166.

[67] J. J. McClelland, A. V. Steele, B. Knuffman, K. A. Twedt, A. Schwarzkopf, and T. M. Wilson, "Bright focused ion beam sources based on laser-cooled atoms," *Applied Physics Reviews,* vol. 3, no. 1, p. 011302, 2016/03/01 2016, doi: 10.1063/1.4944491.

[68] A. Franzen. ComponentLibrary. Available: http://www.gwoptics.org/ComponentLibrary/.

[69] R. Nourshargh, "A Laboratory Atom Interferometer Instrument," Sandia National Lab, 09-01 2018. [Online]. Available: https://doi.org/10.2172/1469758

[70] D. J. McCarron, S. A. King, and S. L. Cornish, "Modulation transfer spectroscopy in atomic rubidium," *Measurement Science and Technology,* vol. 19, no. 10, p. 105601, 2008/08/19 2008, doi: 10.1088/0957-0233/19/10/105601.

[71] E. A. Donley, T. P. Heavner, F. Levi, M. O. Tataw, and S. R. Jefferts, "Double-pass acousto-optic modulator system," *Review of Scientific Instruments,* vol. 76, no. 6, p. 063112, 2005/06/01 2005, doi: 10.1063/1.1930095.

[72] P. Chang, S. Zhang, H. Shang, and J. Chen, "Stabilizing diode laser to 1 Hz-level Allan deviation with atomic spectroscopy for Rb four-level active optical frequency standard,"

Applied Physics B, vol. 125, no. 11, p. 196, 2019/10/04 2019, doi: 10.1007/s00340-019-7313-x.

[73] J. Miao, T. Shi, J. Zhang, and J. Chen, "Compact 459-nm Cs Cell Optical Frequency Standard with $2.1\times10^{-13}/\sqrt{\tau}$ Short-Term Stability," *Physical Review Applied,* vol. 18, no. 2, p. 024034, 08/11/ 2022, doi: 10.1103/PhysRevApplied.18.024034.

[74] G. W. Hoth, E. A. Donley, and J. Kitching, "Atom number in magneto-optic traps with millimeter scale laser beams," *Opt. Lett.,* vol. 38, no. 5, pp. 661-663, 2013/03/01 2013, doi: 10.1364/OL.38.000661.

[75] A. Rakholia, "High Data-Rate Atom Interferometry for Measuring Dynamic Inertial Conditions," Ph.D., University of New Mexico, 2015. [Online]. Available: https://digitalrepository.unm.edu/phyc_etds/55

[76] P. T. Starkey *et al.*, "A scripted control system for autonomous hardware-timed experiments," *Review of Scientific Instruments,* vol. 84, no. 8, p. 085111, 2013/08/01 2013, doi: 10.1063/1.4817213.

[77] C. J. Billington, "State-dependent forces in cold quantum gases," Doctor of Philosophy, School of Physics and Astronomy, Monash University, 2018. [Online]. Available: https://doi.org/10.26180/5bd68acaf0696

[78] P. T. Starkey, "A software framework for control and automation of precisely timed experiments," Doctor of Philosophy, Monash University, 2019. [Online]. Available: https://doi.org/10.26180/5d1db8ffe29ef

[79] R. Ding, "Narrow Line Cooling of ^{84}Sr," Master of Science, Rice University, 2016. [Online]. Available: https://hdl.handle.net/1911/96623

[80] H. J. Lewandowski, D. M. Harber, D. L. Whitaker, and E. A. Cornell, "Simplified System for Creating a Bose-Einstein Condensate," *Journal of Low Temperature Physics,* vol. 132, no. 5, pp. 309-367, 2003/09/01 2003, doi: 10.1023/A:1024800600621.

[81] I. Yavin, M. Weel, A. Andreyuk, and A. Kumarakrishnan, "A calculation of the time-of-flight distribution of trapped atoms," *American Journal of Physics,* vol. 70, no. 2, pp. 149-152, 2002/02/01 2002, doi: 10.1119/1.1424266.

[82] M. Vangeleyn, P. F. Griffin, E. Riis, and A. S. Arnold, "Laser cooling with a single laser beam and a planar diffractor," *Opt. Lett.,* vol. 35, no. 20, pp. 3453-3455, 2010/10/15 2010, doi: 10.1364/OL.35.003453.

[83] C. C. Nshii *et al.*, "A surface-patterned chip as a strong source of ultracold atoms for quantum technologies," *Nature Nanotechnology,* vol. 8, no. 5, pp. 321-324, 2013/05/01 2013, doi: 10.1038/nnano.2013.47.

[84] J. Lee *et al.*, "A compact cold-atom interferometer with a high data-rate grating magneto-optical trap and a photonic-integrated-circuit-compatible laser system," *Nature Communications,* vol. 13, no. 1, p. 5131, 2022/09/01 2022, doi: 10.1038/s41467-022-31410-4.

[85] G. W. Hoth *et al.*, "Towards a compact atomic clock based on coherent population trapping and the grating magneto-optical trap," in *Proc.SPIE*, 2019, vol. 10934, p.

109342E, doi: 10.1117/12.2516612. [Online]. Available: https://doi.org/10.1117/12.2516612

[86] A. Sitaram, P. K. Elgee, G. K. Campbell, N. N. Klimov, S. Eckel, and D. S. Barker, "Confinement of an alkaline-earth element in a grating magneto-optical trap," *Review of Scientific Instruments,* vol. 91, no. 10, p. 103202, 2020/10/01 2020, doi: 10.1063/5.0019551.

[87] S. Bondza, C. Lisdat, S. Kroker, and T. Leopold, "Two-Color Grating Magneto-Optical Trap for Narrow-Line Laser Cooling," *Physical Review Applied,* vol. 17, no. 4, p. 044002, 04/01/ 2022, doi: 10.1103/PhysRevApplied.17.044002.

[88] D. S. Barker, E. B. Norrgard, N. N. Klimov, J. A. Fedchak, J. Scherschligt, and S. Eckel, "Single-Beam Zeeman Slower and Magneto-Optical Trap Using a Nanofabricated Grating," *Physical Review Applied,* vol. 11, no. 6, p. 064023, 06/11/ 2019, doi: 10.1103/PhysRevApplied.11.064023.

[89] *Grating Diffraction Calculator*. (2022).

[90] A. Kawasaki, B. Braverman, Q. Yu, and V. Vuletic, "Two-color magneto-optical trap with small magnetic field for ytterbium," *Journal of Physics B: Atomic, Molecular and Optical Physics,* vol. 48, no. 15, p. 155302, 2015/06/26 2015, doi: 10.1088/0953-4075/48/15/155302.

[91] J. Lee, G. Biedermann, J. Mudrick, E. A. Douglas, and Y.-Y. Jau, "Demonstration of a MOT in a sub-millimeter membrane hole," *Scientific Reports,* vol. 11, no. 1, p. 8807, 2021/04/22 2021, doi: 10.1038/s41598-021-87927-z.

[92] A. Goban *et al.*, "Atom-light interactions in photonic crystals," *Nature Communications,* vol. 5, no. 1, p. 3808, 2014/05/08 2014, doi: 10.1038/ncomms4808.

[93] D. E. Chang, J. S. Douglas, A. González-Tudela, C. L. Hung, and H. J. Kimble, "Colloquium: Quantum matter built from nanoscopic lattices of atoms and photons," *Reviews of Modern Physics,* vol. 90, no. 3, p. 031002, 08/01/ 2018, doi: 10.1103/RevModPhys.90.031002.

LABORATORY DIRECTED RESEARCH & DEVELOPMENT

WHERE INNOVATION BEGINS

ADDENDUM:

The slides below were presented to the LDRD committee prior to discovering an error in the pixel size calibration analysis, resulting in erroneous time-of-flight temperatures. This error was corrected and the data reanalyzed in the main body of the text but the slides below are included for completeness.

Narrow-linewidth laser cooling for rapid production of low-temperature atoms for high data-rate quantum sensing, LDRD #222387

Roger Ding (5228, PI), Adrian Orozco (5228), Jongmin Lee (5228), Neil Claussen (5228, PM)

Purpose, Approach, and Goal

Purpose: fast production of cold atoms for quantum sensing applications (e.g., atom interferometers, atomic clocks) while keeping them trapped by bypassing sub-Doppler cooling stage

Standard approach: broad linewidth 780 nm magneto-optical trap (MOT) with sub-Doppler cooling

New approach: narrow linewidth 420 nm MOT to directly achieve lower temperatures while keeping atoms trapped

- Was demonstrated for Li and K (Rb [1] occurred during this LDRD)

Key goal: demonstrate a MOT using the 420 nm transition in rubidium and show it is colder than the standard 780 nm MOT

Representative Figure

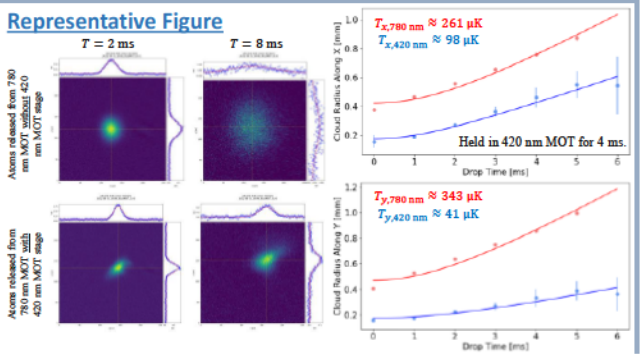

Key R&D Results and Significance

Summarize your R&D

Recently demonstrated first 420 nm MOT at Sandia!

The result for the one key goal

Current 420 nm MOT is weak but already showing temperatures below 780 nm Doppler cooling limit (i.e., $T_{420\,\mathrm{nm}} < T_{D,780\,\mathrm{nm}} \approx 146\ \mu\mathrm{K}$)

Lessons learned

- 420 nm MOT *is* a viable approach but needs more investigation
- Reviving an old experimental system was… challenging
- Should have invested significant efforts into modeling MOT

Follow-on plans/activities

- 420 nm Raman for $\gtrsim 1.8\times$ increase in atom interferometer sensitivity
  - Demonstrating 420 nm Raman alone could be a publication
- Pure 420 nm MOT w/o 780 nm repump (possible publication)
- 420 nm grating MOT (builds on results from SIGMA-GC)

Impact of follow-on plans

No direct follow-on plans but results can easily open new avenues of research within upcoming LDRDs

Publications, awards, staff development & IP

- No publication plans since another group beat us by ~6 months [1]
- Staff development:
  - Supported RD and AO for ~ 60% time over ~4 months
  - AO converted from graduate student to postdoc during project

LABORATORY DIRECTED RESEARCH & DEVELOPMENT

WHERE INNOVATION BEGINS

R&D Summary (Introduction)

Rapid and reliable generation of cold atoms is critical for moving quantum sensors from well-controlled laboratory environments to the field

- Magneto-optical traps (MOTs) are *the* tool for producing cold clouds of atoms but limited to $T_D = \hbar\Gamma/2k_B$ (Doppler cooling limit)
- Remaining atomic motion (i.e., temperature) is still detrimental

Focus on ^{87}Rb but approach is applicable to other atomic species (e.g., ^{133}Cs)

- Widely-used for current quantum sensing research at Sandia and abroad
  - Atom interferometers, magnetometers, quantum simulation/information, etc.

Current state-of-the-art: $5S_{1/2} \rightarrow 5P_{3/2}$ MOT at 780 nm

- $\Gamma_{780\,\mathrm{nm}} = 2\pi(6.1\ \mathrm{MHz}) \Rightarrow T_D \approx 146\ \mu\mathrm{K}$
- Sub-Doppler cooling can reach $T \approx 5\ \mu\mathrm{K}$ but:
  - Sensitive to stray magnetic fields
  - Atoms are not trapped during sub-Doppler cooling

New approach: $5S_{1/2} \rightarrow 6P_{3/2}$ MOT at 420 nm

- $\Gamma_{420\,\mathrm{nm}} \lesssim 2\pi(1.4\ \mathrm{MHz}) \Rightarrow T_D \lesssim 34\ \mu\mathrm{K}$
- Atoms in a 420 nm MOT remain trapped!

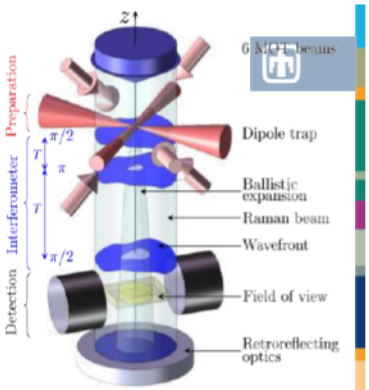

Illustration of cold atom cloud expanding during atom interferometer pulses, experiencing inhomogeneities of Raman beam [2].

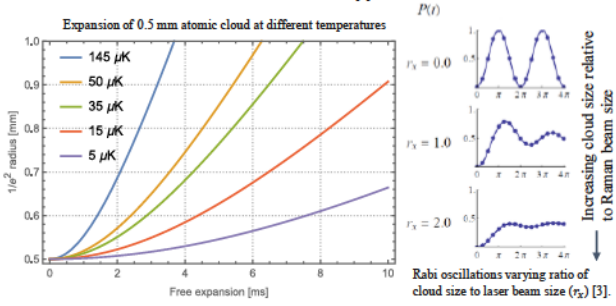

Rabi oscillations varying ratio of cloud size to laser beam size (r_x) [3].

LABORATORY DIRECTED RESEARCH & DEVELOPMENT

WHERE INNOVATION BEGINS

R&D Summary (Methods)

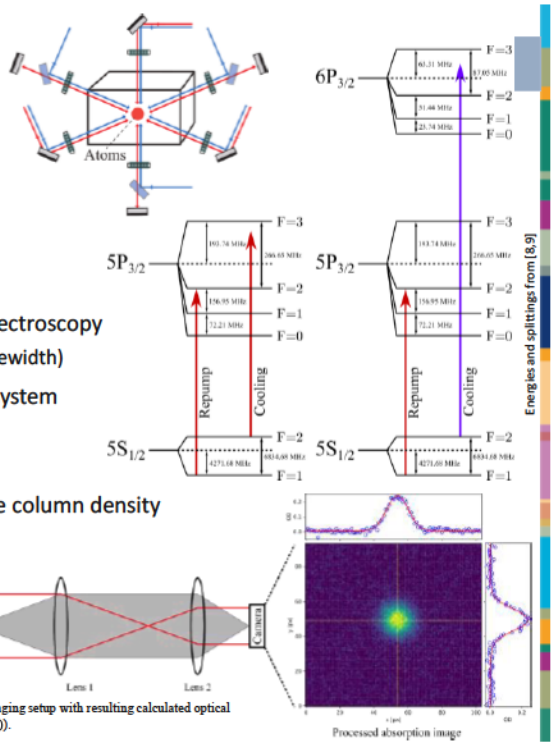

Revive an existing experimental system for 780 nm MOT ^{87}Rb [4]

- Upgrade to Python-based experiment control system [5]
- Augment system with absorption imaging [6] capability

Add 420 nm laser system to experiment

- Stabilize 420 nm laser to atomic transition using Doppler-free spectroscopy
  - The $|5S_{1/2}, F = 2\rangle \rightarrow |6P_{3/2}, F = 3\rangle$ transition is weak (narrow linewidth)
- Make 420 nm MOT laser system and overlap with 780 nm MOT system

Main diagnostic tools

- Absorption imaging [6]: take pictures of atomic cloud to calculate column density

$$n(x,y) = \frac{1}{\sigma_0} I_{\mathrm{OD}}(x,y) = \frac{1}{\sigma_0} \ln\left[\frac{I_{\mathrm{bright}}(x,y) - I_{\mathrm{dark}}(x,y)}{I_{\mathrm{atoms}}(x,y) - I_{\mathrm{dark}}(x,y)}\right]$$

- Time-of-flight (ToF) [7]: vary drop time (t_{Drop}) to obtain cloud temperature (T):

$$r(t_{\mathrm{Drop}}) = \sqrt{r(t_{\mathrm{Drop}} = 0)^2 + \frac{k_B T}{M} t_{\mathrm{Drop}}^2}$$

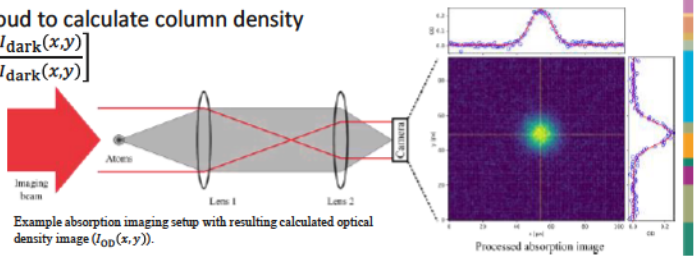

Example absorption imaging setup with resulting calculated optical density image ($I_{\mathrm{OD}}(x,y)$).

LABORATORY DIRECTED RESEARCH & DEVELOPMENT

WHERE INNOVATION BEGINS

R&D Summary (Results)

Upgraded experimental control system

- Previous: FPGA with custom code to control experiment but little documentation
- Now: Python-based labscript control system [5] with code tracking on CEE GitLab
  - Documented experiment and system; self-contained HDF5 data files incorporates relevant information

Stabilized 420 nm laser to the weak $|5S_{1/2}, F = 2\rangle \rightarrow |6P_{3/2}, F = 3\rangle$ transition

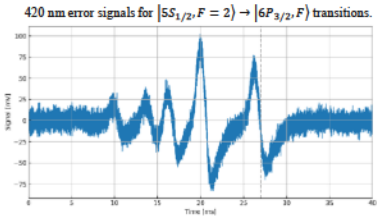

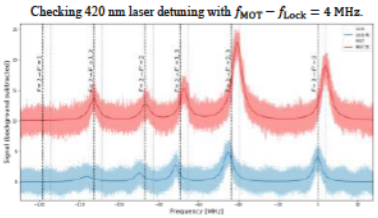

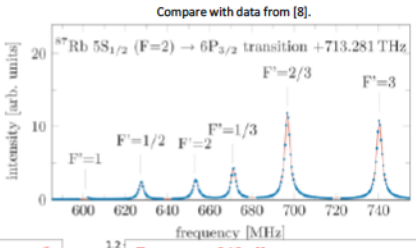

Demonstrated the first 420 nm ^{87}Rb MOT at Sandia!

- 420 nm MOT temperature already below 780 nm Doppler limit ($T_{D,780\,\mathrm{nm}} \approx 146\ \mu\mathrm{K}$)!

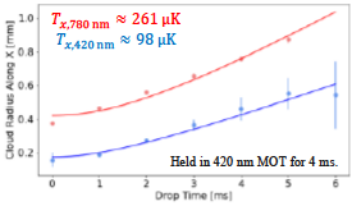

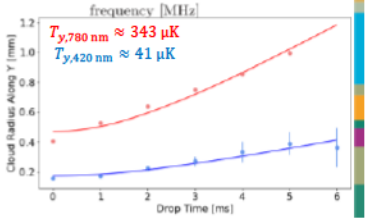

Still lots of optimization/characterization to do

LABORATORY DIRECTED
RESEARCH & DEVELOPMENT
WHERE INNOVATION BEGINS

R&D Summary (Results)

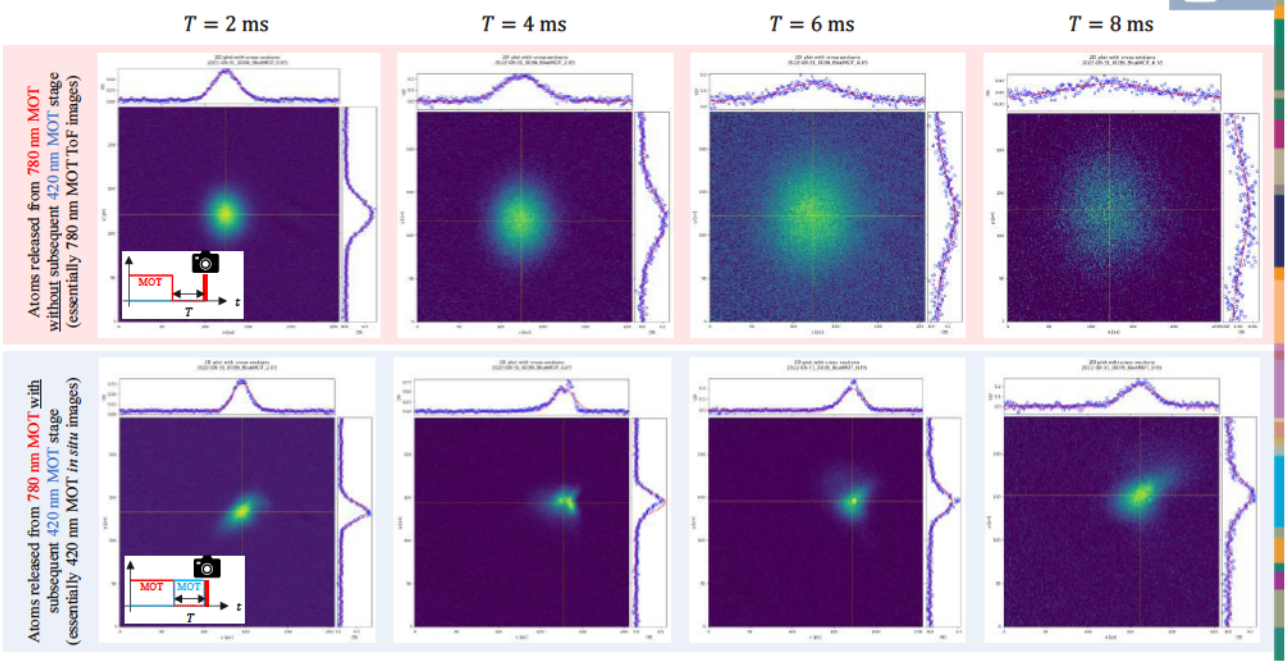

LABORATORY DIRECTED RESEARCH & DEVELOPMENT

WHERE INNOVATION BEGINS

R&D Summary (Discussions)

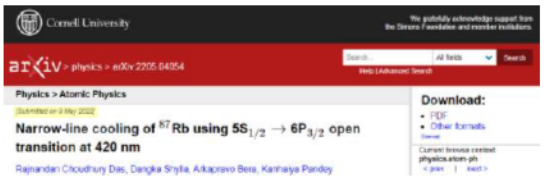

Some disappointment: another group beat us to "publishing" on the 420 nm ^{87}Rb MOT

- arXiv preprint submitted on May 9, 2022 [1]
- Our 420 nm laser arrived on May 24, 2022

Lessons learned

- 420 nm ^{87}Rb MOT *is* a viable approach but needs more investigation
- Reviving the old experimental system caused quite a few headaches and problems…
- 420 nm lock works but could be significantly better to improve long-term stability
- Did not observe 420 nm MOT trapping from atomic vapor, needed to load from 780 nm MOT
  - Would require investing serious efforts into modeling 3D MOT (challenging due to multiple m_F-levels)
  - Using small MOT 420 nm beams ($\approx 3.5 \times 5\ \mathrm{mm}^2$) leads to unfavorable atom number scaling [10]

Potential future directions

- Demonstrate 420 nm Raman for atom interferometry: $\sigma_a = \delta\phi/(ak_{\mathrm{eff}}T^2)$ where $k_{\mathrm{eff}} \approx 2(2\pi/\lambda)$
  - $k_{\mathrm{eff,420\ nm}}/k_{\mathrm{eff,780\ nm}} \approx 1.86$ meaning almost twice as sensitive to acceleration for same free-evolution time T
- Purely 420 nm MOT without 780 nm repump could potentially be a publication ([1] used 780 nm repump)
- 420 nm grating MOT: leverage systems and tools developed during SIGMA Grand Challenge

LABORATORY DIRECTED RESEARCH & DEVELOPMENT

WHERE INNOVATION BEGINS

LDRD Project Metrics

Presentations and Publications

- Had planned on a publication until the Das et al. arXiv preprint [1]

Intellectual Property

Tools and Capabilities

- Revived a legacy laser system for laser cooling Rb, will be used for upcoming funded LDRD(s)
- Implemented labscript experimental control system, will be used for upcoming funded LDRD(s)
- Demonstrated capability to perform absorption imaging and utilize associated analysis techniques

Staff Development

- Supported RD (postdoc) and AO (graduate student to postdoc) for ~ 60% time over ~4 months
- For myself (RD): a major learning experience

Awards

LABORATORY DIRECTED RESEARCH & DEVELOPMENT

WHERE INNOVATION BEGINS

Project Legacy

Key Technical Accomplishment

- Observed first 420 nm ^{87}Rb MOT at Sandia! (but still have a lot of optimization/characterization to do)

How does this engage Sandia missions?

- Methods for rapid generation of cold atoms will be important for developing future quantum sensor technologies
- Would eventually leverage fab capability for chip-based laser sources, modulators, delivery to atoms, etc.

Plans for follow-on and partnerships?

- Unfortunately, no direct follow-on plans as technique needs more investigation
  - Could easily augment existing/upcoming LDRDs with different research avenues
- Close to getting publishable results but would need some more time and equipment
  - 420 nm-only MOT or 420 nm grating MOT would be most straightforward directions

What do you wish you could have done, but didn't?

- (Besides being aware of the experimental challenges from the start…)
- Started reviving the existing 780 nm system earlier (lots of issues needed to be fixed)
- Switched to trapping ^{85}Rb instead of ^{87}Rb due to larger natural abundance (^{85}Rb: 72.17% vs. ^{87}Rb: 27.83%)
- Invested significant effort into modeling 420 nm MOT (24 F-states and each F state has $(2F + 1)$ m_F-states)

Picture of the experimental setup

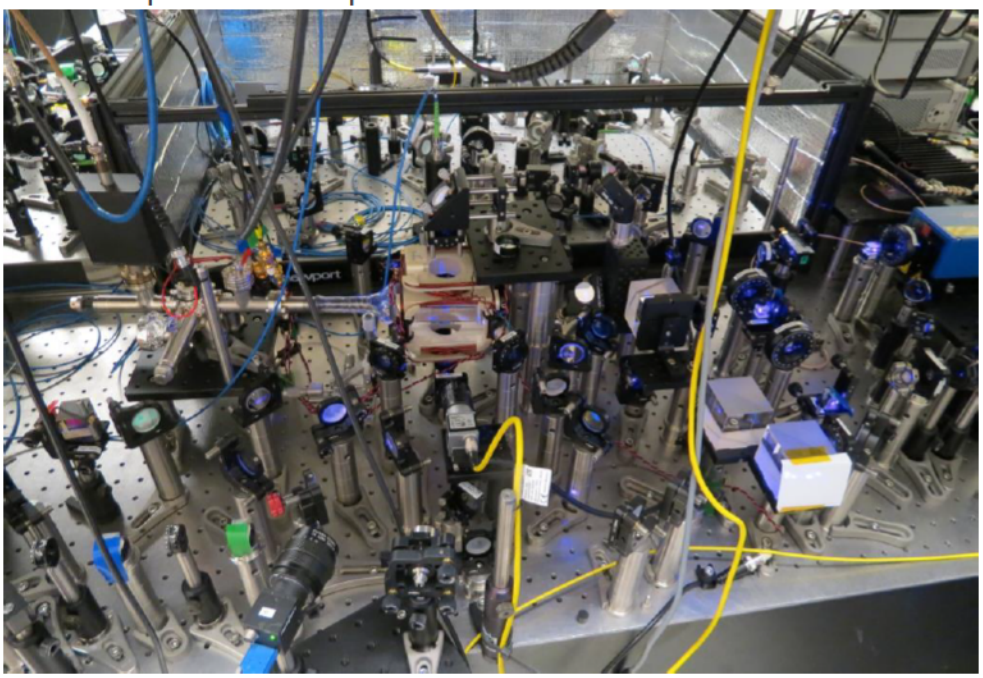

Some of the challenges

- **Supply chain issues!!**
  - Laser arrived late in FY22 (ordered in November 2021)
  - Lead times to buy equipment for working around challenges
- Poor 420 nm beam quality output from laser
  - Difficult to align and "balance" 420 nm MOT forces
  - Fiber-coupling would clean-up mode (but $$$ and mW)

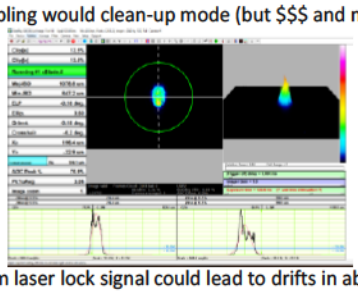

- Weak 420 nm laser lock signal could lead to drifts in absolute frequency
  - E.g., due to AOM beam pointing and/or power drifts
  - Electro-optic modulator (EOM) would likely produce cleaner and larger signal (but $$$)
- A more sensitive camera would produce stronger absorption imaging signals
  - Used a standard CCD camera (from Reapp)

- UHV glass cell was antireflection (AR) coated for 780 nm but had *very* poor transmission for 420 nm
  - ~ 14% loss per glass wall at 420 nm!

λ [nm]	P_{In} [mW]	P_{Out} [mW]	$T = \left(\frac{P_{Out}}{P_{In}}\right)^{\frac{1}{2}}$
780	4.07	3.7	0.953463
420	6.5	3.8	0.764601

- Required drastic change-of-plans from a simple 3-beam retroreflected MOT to a 6-independent-beam MOT
  - Used 50:50 (from Reapp) to make 6 beams from 3
  - Borrowed additional dichroic beam combiners and optics
- Vertical MOT axis could still experience some antitrapping forces due to surface reflections

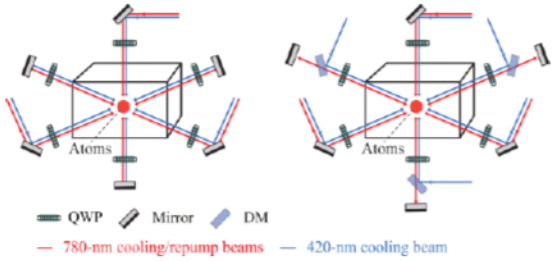

LABORATORY DIRECTED RESEARCH & DEVELOPMENT

WHERE INNOVATION BEGINS

Labscript control system

- Labscript is a flexible and extensible Python-based control system [5] with analysis code tracked on CEE GitLab
  - Works with commercial-off-the-shelf components including:
    - SpinCore PulseBlaster for main experimental timing
    - National Instruments signal output and input (ADCs, DACs, etc.)
    - Basler and Teledyne/FLIR cameras
  - Can queue multidimensional "shots" (experimental runs) and stores results in HDF5 files
  - Under active development (so we do occasionally run into bugs, missing features, etc.)

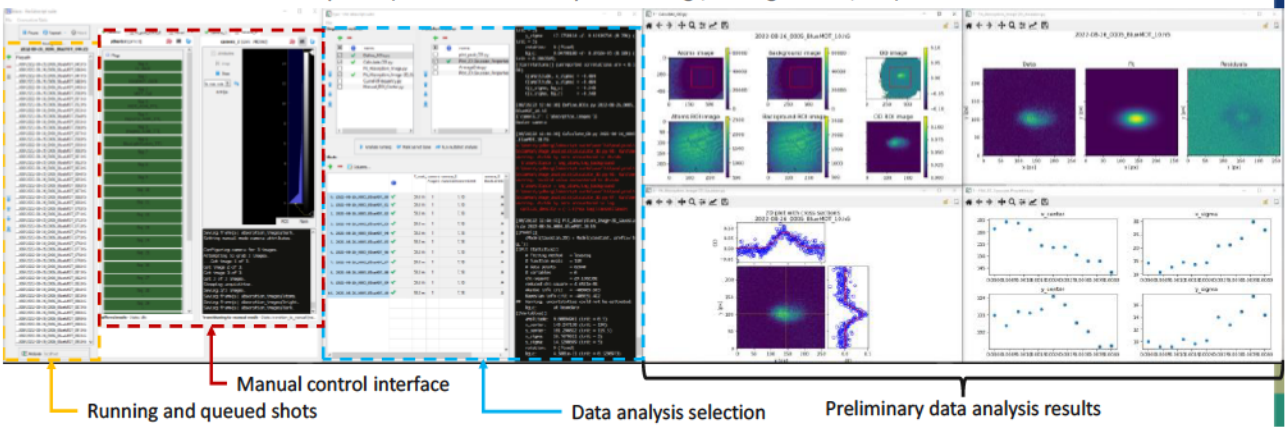

LABORATORY DIRECTED RESEARCH & DEVELOPMENT

WHERE INNOVATION BEGINS

Additional details about ^{87}Rb 780 nm and 420 nm transitions

- 780 nm MOT drives $|5S_{1/2}, F = 2\rangle \rightarrow |5P_{3/2}, F = 3\rangle$ closed transition
  - $1/\tau_{5P_{3/2}} = 26$ ns $\Rightarrow \Gamma_{780\text{ nm}} \approx 2\pi(6.1\text{ MHz})$
  - $T_{D,780\text{ nm}} \approx 146\ \mu$K
- 420 nm MOT drives $|5S_{1/2}, F = 2\rangle \rightarrow |6P_{3/2}, F = 3\rangle$ open transition
  - $1/\tau_{5S_{1/2}\rightarrow 6P_{3/2}} = 500$ ns so would expect $\Gamma_{420\text{ nm}} \approx 2\pi(320\text{ kHz})$
  - But decay cascade reduces $6P_{3/2}$ lifetime to $1/\tau_{6P_{3/2}} = 112$ ns $\Rightarrow \Gamma_{420\text{ nm}} \approx 2\pi(1.4\text{ MHz})$
  - $T_{D,420\text{ nm}} \lesssim 34\ \mu$K

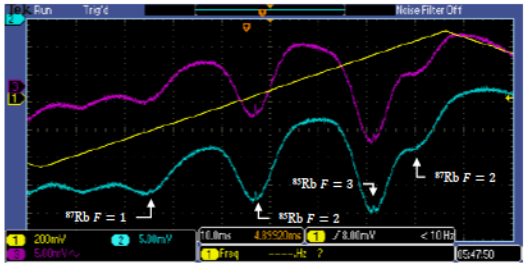

Doppler-free absorption features from $5S_{1/2} \rightarrow 6P_{3/2}$ at 420 nm.

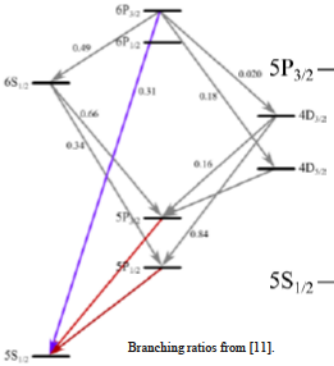

Branching ratios from [11].

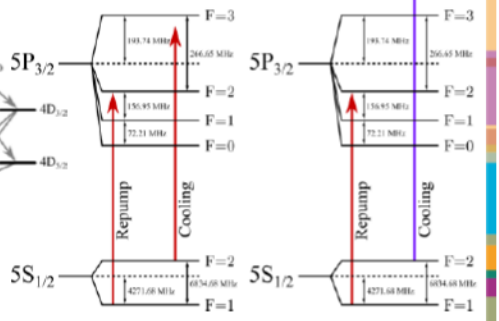

Energies and splittings from [8, 9].

LABORATORY DIRECTED RESEARCH & DEVELOPMENT

WHERE INNOVATION BEGINS

A little about magneto-optical traps (MOTs)

- 1997 Nobel Prize: Chu, Cohen-Tannoudji, Phillips
- Magneto-optical traps (MOTs)
  - Need:
    - Quadrupole magnetic field to define trap center
    - 6 counterpropagating circularly-polarized beams tuned slightly below resonance of a cycling transition
  - Result:
    - Position-dependent force due to Zeeman shift in quadrupole magnetic field = trapping
    - Velocity-dependent (viscous damping) force due to Doppler-shift of laser tuned below resonance = cooling
  - For ^{87}Rb (and other alkali atoms): a repump laser closes a leak to the lower hyperfine state ($5S_{1/2}, F = 1$) that is dark to the cooling light

Grating magneto-optical trap (GMOT) [12]

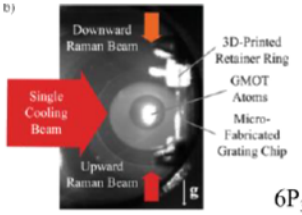

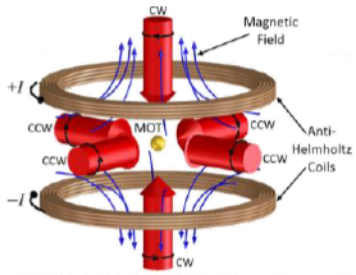

3D MOT schematic from [13].

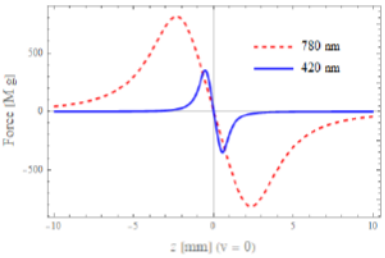

1D MOT force calculation for 780 nm ($\Gamma_{780\text{ nm}} = 2\pi(6\text{ MHz})$) and 420 nm ($\Gamma_{420\text{ nm}} = 2\pi(1.4\text{ MHz})$) assuming $\Delta = -\Gamma/2$, $dB/dz = 10$ G/cm, and $s = 0.1$.

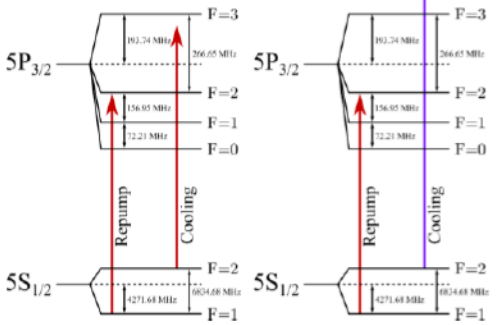

Energies and splittings from [8, 9].

Absorption imaging

Principle: atoms scatter light out of a (near-)resonant laser beam, casting a shadow on a sensor [6]

- Take three (3) images:
  1. $I_{\text{atoms}}(x,y)$: flash on imaging beam to capture picture of atom cloud
  2. $I_{\text{bright}}(x,y)$: flash on imaging beam without the atom cloud to get picture of imaging beam intensity distribution
  3. $I_{\text{dark}}(x,y)$: picture without atom cloud nor imaging beam
- Calculate optical density $I_{\text{OD}}(x,y) = \ln\left[\frac{I_{\text{bright}}(x,y) - I_{\text{dark}}(x,y)}{I_{\text{atoms}}(x,y) - I_{\text{dark}}(x,y)}\right]$
- Extract relevant parameters using $I_{\text{OD}}(x,y) = \sigma_0 n(x,y)$
  - $n(x,y)$ is the column density (i.e., density $n(x,y,z)$ integrated along imaging beam $\boldsymbol{k} = k\hat{z}$)
  - σ_0 is the absorption cross section

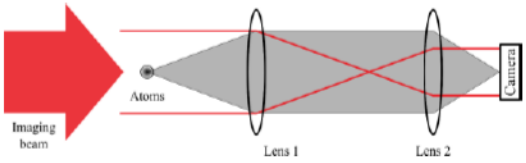

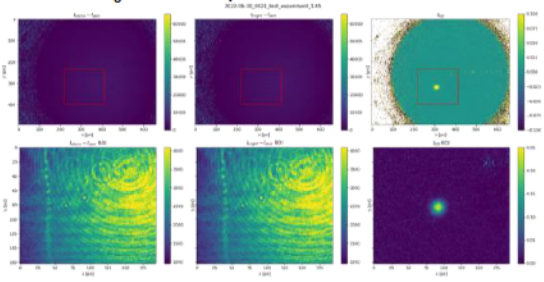

Image analysis (e.g., 2D Gaussian fit)

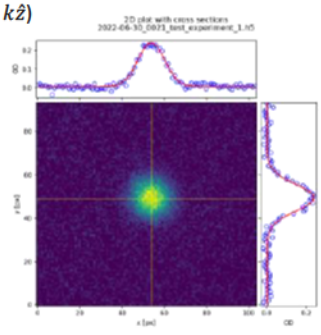

Time-of-flight (ToF) measurement

Principle: turning off all trapping fields allows atoms to ballistically expand, mapping initial momentum distribution to a position distribution [7]

- Taking an absorption imaging captures the atom position distribution
- Vary the time delay t_{Drop} between turning off trapping fields and absorption imaging
  - Can extract pixel-to-meter conversion from falling cloud: $y(t_{\mathrm{Drop}}) = y_0 + \frac{1}{2} g t_{\mathrm{Drop}}^2$
- Fit $I_{\mathrm{OD}}(x, y)$ image to extract cloud size (r) vs. drop time (t_{Drop})
  - For a thermal cloud with an initial Gaussian width r_0: $r(t_{\mathrm{Drop}}) = \sqrt{r_0^2 + \frac{k_B T}{M} t_{\mathrm{Drop}}^2}$
- Extract temperature (T) by fitting $r(t_{\mathrm{Drop}})$

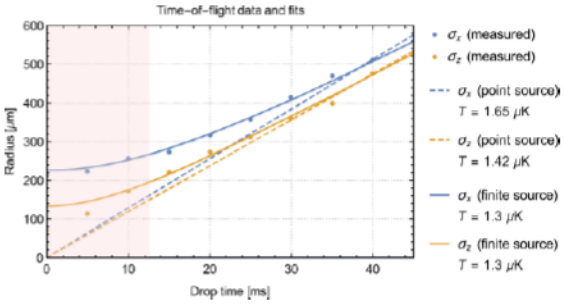

Fitting $\sigma(t_{\mathrm{Drop}})$

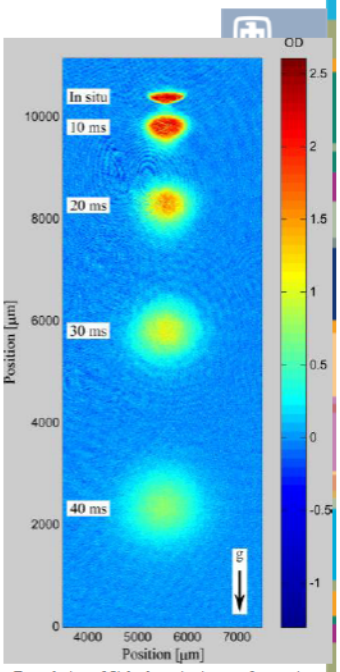

Example time-of-flight absorption images of a strontium 689 nm MOT at $T \approx 1.4$ μK.

References

[1] R. C. Das et al., arXiv:2205.04054; https://doi.org/10.48550/arXiv.2205.04054

[2] R. Karcher et al., New J. Phys. **20** 113041 (2018); https://doi.org/10.1088/1367-2630/aaf07d

[3] Akash Rakholia, "High Data-Rate Atom Interferometry for Measuring Dynamic Inertial Conditions", PhD (2015); http://hdl.handle.net/1928/30412

[4] Rustin Nourshargh, "A Laboratory Atom Interferometer Instrument", MS (2018); https://doi.org/10.2172/1469758

[5] P. T. Starkey et al., Review of Scientific Instruments **84**, 085111 (2013); https://doi.org/10.1063/1.4817213

[6] H. J. Lewandowski et al., Journal of Low Temperature Physics **132**, 309–367 (2003); https://doi.org/10.1023/A:1024800600621

[7] I. Yavin et al., American Journal of Physics **70**, 149-152 (2002); https://doi.org/10.1119/1.1424266

[8] C. Glaser et al., Phys. Rev. A **102**, 012804 (2020); https://doi.org/10.1103/PhysRevA.102.012804

[9] Daniel A. Steck, ''Rubidium 87 D Line Data,'' available online at http://steck.us/alkalidata

[10] G. W. Hoth et al., Opt. Lett. **38**, 661-663 (2013); https://doi.org/10.1364/OL.38.000661

[11] O. S. Heavens, J. Opt. Soc. Am. **51**, 1058-1061 (1961); https://doi.org/10.1364/JOSA.51.001058

[12] J. Lee et al., Nat Commun **13**, 5131 (2022); https://doi.org/10.1038/s41467-022-31410-4

[13] J. J. McClelland et al., Applied Physics Reviews **3**, 011302 (2016); https://doi.org/10.1063/1.4944491